SANDIA REPORT
SAND2006-5934
Unlimited Release
Printed October 2006

Studies of Signaling Domains in Model and Biological Membranes through Advanced Imaging Techniques: Final Report

Alan R. Burns, Janet M. Oliver, Bridget S. Wilson, and Janet R. Pfeiffer

Prepared by
Sandia National Laboratories
Albuquerque, New Mexico 87185 and Livermore, California 94550

Sandia is a multiprogram laboratory operated by Sandia Corporation,
a Lockheed Martin Company, for the United States Department of Energy's
National Nuclear Security Administration under Contract DE-AC04-94AL85000.

Issued by Sandia National Laboratories, operated for the United States Department of Energy by Sandia Corporation.

Available to DOE and DOE contractors from
U.S. Department of Energy
Office of Scientific and Technical Information
P.O. Box 62
Oak Ridge, TN 37831

Telephone: (865) 576-8401
Facsimile: (865) 576-5728
E-Mail: reports@adonis.osti.gov
Online ordering: http://www.osti.gov/bridge

Available to the public from
U.S. Department of Commerce
National Technical Information Service
5285 Port Royal Rd.
Springfield, VA 22161

Telephone: (800) 553-6847
Facsimile: (703) 605-6900
E-Mail: orders@ntis.fedworld.gov
Online order: http://www.ntis.gov/help/ordermethods.asp?loc=7-4-0#online

SAND 2006-5934
Unlimited release
Printed October 2006

Studies of Signaling Domains in Model and Biological Membranes through Advanced Imaging Techniques: Final Report

Alan R. Burns
Biomolecular Interfaces and Systems Department
P.O. Box 5800
Sandia National Laboratories
Albuquerque, NM 87185-1413

Janet M. Oliver, Bridget S. Wilson, and Janet R. Pfeiffer
Department of Pathology and Cancer Center
University of New Mexico
School of Medicine
Albuquerque, NM 87131

ABSTRACT

Cellular membranes have complex lipid and protein structures that are laterally organized for optimized molecular recognition and signal transduction processes. Knowledge of nanometer-scale lateral organization and its function is of great importance in the analysis of receptor-based signaling. In model membranes, we studied in detail the chemical and physical factors which result in lateral organization of lipids and lipid-mediated protein sequestration into signaling domains. In biological membranes, we mapped the location and follow the dynamic activity of specific membrane proteins involved in the immunological response of mast cells. These studies were enabled by our development of advanced imaging methods that provided both high spatial resolution and sensitivity to dynamical processes. Our technical approach was to combine the high sensitivity and time resolution of fluorescence imaging with the high lateral resolution of atomic force microscopy (AFM). Simultaneous fluorescence and AFM imaging allows correlation of the distribution and dynamic activity of specific biomolecules via fluorescence labeling with complete topographic information of the membrane. Overall, our unique imaging capabilities enabled us to examine membrane structure and function with much greater detail than was previously possible and thus provide a better understanding of cellular signaling.

(this page intentionally left blank)

Contents

(this page intentionally left blank)

1. Introduction

Membranes are fundamental components of all cellular organisms. Not only does the membrane enclose each cell as a separate biological entity, but it performs a myriad of critical functions to maintain the life of the cell with respect to the "extracellular," or outside, world. Despite the enormous variety of life forms, biological membranes have a common basic structure that is composed of a thin (~6.0 nm) film of lipids and proteins. For many years it was thought that the fluid-like behavior of the lipids resulted in a structureless assembly that simply formed an impermeable wall. However, it is now clear that the lipids, in concert with the membrane proteins, can be organized into structures that help the cell perform specific functions.

The lipids form a bilayer that incorporates many transmembrane proteins, as well as many membrane associated proteins. Domains of lipids may form within the bilayer due to subtle differences in molecular structure. Many believe that these "lipid rafts" may in turn serve to sequester specific groups of proteins that perform specific functions. Others believe that the proteins cluster due to protein-protein interactions and organize the lipids around them. In any case, *model membranes* were used here to examine the fundamental aspects of lipid domains. The lipid bilayer model membranes also served to refine the imaging techniques that were subsequently used in biological cell membranes.

One of the most important functions of the membrane is that of "cellular signaling," the process by which "receptor" proteins in the membrane detect specific biomolecules in the extracellular environment and trigger a response by the cell. In collaboration with the Dept. of Pathology at the University of New Mexico, Sandia developed advanced imaging techniques to map the location of receptor proteins and associated protein partners in the signaling network. Specifically, we use atomic force microscopy (AFM), combined with fluorescence labeling, to map the location of receptor proteins within the topographical structure of the cytoplasmic (interior) side of mast cell membranes. Mast cells are involved in the adaptable immune response that ultimately results in the expression of histamines.

The cell is the ultimate biosensor. Just a few antigens bound to receptor proteins can induce a cascade of cellular processes which can take many years to deduce. We can learn much about biosensing from fundamental studies in cell membrane structure and function. Moreover, medical advances in cancer research and drug therapies will depend to a large extent on a molecular-level understanding of cellular signaling at the membrane.

(this page intentionally left blank)

2. Summary of Accomplishments

2.1 Model membrane studies

2.1.1 Domain structure

In the first two publications included for this report, we used simultaneous atomic force microscopy (AFM) and confocal fluorescence imaging to examine simple lipid domains in two-component lipid mixtures. The first publication (*Langmuir* 2003, **19**, 8358-8363) is focused on domain structure and probe portioning. Although it predates the LDRD, it is included here because it explains the detailed experimental techniques and sample preparation protocols that were used and refined during the course of the LDRD project.

AFM/fluorescence imaging of 1,2-dipalmitoyl-sn-glycero-3-phosphocholine (DPPC) lipid domain structures in 1,2-dioleoyl-sn-glycero-3-phosphocholine (DOPC) was performed. Lipids labeled by fluorescent probes either at the headgroups or tailgroups enable domain contrast in fluorescence imaging on the basis of partitioning between the gel (DPPC) and disordered liquid (DOPC) phases. The simultaneous acquisition of fluorescence and AFM topographic information provides insights on lateral organization that either technique alone would not necessarily be able to provide. Well-defined gel-phase DPPC domains with irregular shapes and sizes ranging from 10 nm up to several microns were observed in AFM images on the basis of the ~1 nm height difference above the surrounding DOPC fluid-phase. In the fluorescence images, those same (resolvable) domains were observed by the selective partitioning of probe-labeled lipids for the liquid-phase.

Correlation between the two sets of images revealed that the fluorescent probe lipid partitioning was not uniform across the domains, thus potentially distorting domain size and shape beyond that imposed by optical resolution. Furthermore, we found that the fluorescence contrast decreases significantly with domain size, such that small domains observed with AFM were not observed in fluorescence images despite adequate optical resolution. We attribute these effects in part to broadened partitioning of the probe lipids across the domain boundaries. Binding of fluorescent Alexa 488-conjugated cholera toxin B subunits to GM1 gangliosides in DPPC domains correlates well with AFM topographic information to the limit of optical resolution. However, it also may reveal the presence of dilute GM1 components in the fluid phase that have no topographic contrast. In all cases, the complete correlation of topographic and fluorescence images provides evidence that gel-phase domains occur across both leaflets of the bilayer.

2.1.2 Local mobility in lipid domains

In the second publication (*Biophysical Journal* 2005, **89**, 1081-1093), fluorescence correlation spectroscopy (FCS) was used to examine mobility of labeled probes at specific sites in supported bilayers consisting of the same DPPC lipid domains in DOPC. Those sites were mapped beforehand with simultaneous AFM/fluorescence imaging, allowing characterization of probe partitioning between gel DPPC and disordered liquid DOPC domains with corresponding

topography of domain structure. We thus examined the relative partitioning and mobility in gel and disordered liquid phases for headgroup- and tailgroup-labeled GM1 ganglioside probes, and for headgroup- and tailgroup-labeled phospholipid probes. The four probes were chosen because they are fluorescent analogs of naturally occurring lipids and they represent two common labeling schemes requiring headgroup and tailgroup modification. Overall, we found that the supported model membranes have common attributes in structure and fluidity with unsupported vesicles; however, we have also presented unexpected results that suggest possible fluorophore effects on probe partitioning, domain heterogeneity, and probe mobility.

Partitioning is an important aspect of lipid "raft" models We saw that the exclusion of labeled probes by their unlabeled counterparts in gel domains was indicative of significant perturbations in packing and/or lipid interactions, consistent with previous studies on supported and unsupported model membranes. For both headgroup- and tailgroup-labeled saturated phospholipid analogs, we saw that modifications in either the acyl chain or the head group lead to exclusion from the saturated gel domains. For the GM1 analogs, we found that tail-group labeled GM1 was excluded from the gel domains, whereas headgroup-labeled GM1 was not excluded. Thus the presence of the fluorescent label on the asialoganglioside head group does not interfere with the interactions that allow GM1 to occupy sites in the gel phase DPPC.

Equally important in the lipid raft model of membrane function is the mobility of the lipid components inside and outside domains. Overall, we found that the mobilities of all four probes were roughly the same in the DOPC fluid phase. Thus we found no glaring difference in fluid phase mobility due to the location of the head or tail group labeling. Both tailgroup-labeled GM1and unmodified GM1 were shown to slow down by at least a factor of six upon binding to cholera toxin B (CTX-B) fragments, which most likely indicates clustering induced by the pentameric CTX-B. Mobility of the unbound GM1 analogs was severely attenuated in the gel phase DPPC. This was definitely the case for the headgroup-labeled GM1, indicating a tight packing by the surrounding DPPC lipids. Furthermore, mobility appeared to be restricted around the domain boundaries. The mobility in DPPC was also restricted for tailgroup-labeled GM1, however evidence was presented for increased mobility in submicron domains that may be due to DPPC packing heterogeneities. Mobility around the domain boundaries was higher, resembling, for the most part, that in the fluid phase.

This trend of increasing mobility in and around the submicron DPPC domains was remarkably prevalent in the tailgroup-labeled and headgroup-labeled phospholipid analogs. For these probes there appeared to be little reduction in the lateral diffusion in the submicron DPPC domains relative to the DOPC regions. The results for submicron domains may be relevant to mobility in sphingolipid-cholesterol domains in biological membranes, where domain sizes are believed to less than 100 nm. Thus its appears that those lipids such as headgroup-labeled GM1 and unmodified GM1 that partition into the DPPC domains do not disrupt the dense packing and thus are rendered immobile. Whereas those lipids that are excluded on the basis of disrupting the gel packing and/or lipid-lipid interactions may have greater mobility.

We were able to show that FCS can reveal heterogeneities in supported lipid bilayers. The phospholipid probes not only exhibited a perplexing mobility in submicron DPPC domains, but also required two-component fits to the FCS curves in the fluid DOPC phase. The slow

component could be due to variety of factors including substrate interactions and membrane heterogeneities. However, it could also be due to local distortion of the molecule and surrounding matrix lipids by the tendency of fluorophores to seek polar regions of the membrane. This effect may also be responsible for exclusion of the probes from close-packed gel domains. In any case, it is clear that the phospholipid probes, as well as other labeled phospholipid lipids using different fluorophores, are not ideal for the modeling of partitioning and mobility in membranes. They do, however, illustrate that lipid components and lipid-protein complexes in biological membranes could move rapidly in and out of raft domains as needed.

2.2 Signaling domains in mast cell membranes

Immunogold labeling and transmission electron microscopic (TEM) imaging work at UNM of endogenous proteins in the cytoplasmic face of mast cell membranes, including the abundant IgE receptor (FcεRI) and its signaling partners, has revealed that most proteins in native membranes are dispersed prior to stimulus. Since the cell membrane is adaptable and capable of dynamic reorganization, the FcεRI can coalesce within minutes of activation into patches as large as 200-400 nm in diameter. Because these sites of receptor aggregation accumulate many signaling proteins, they are presumed to be sites of active signaling. The signaling patches typically occupy "dark" membrane regions that show enhanced labeling with osmium, indicating high levels of double bond-containing lipids and/or cholesterol, and are frequently bordered by clathrin-coated pits. It was of great interest, therefore, to determine if the signaling patches are indeed distinct topographic features in mast cell membranes.

Thus we used AFM/fluorescence imaging to examine the topography of the cytoplasmic face of plasma membrane sheets stripped from tumor mast cells (RBL-2H3). This work is included here as the third publication (*Biophysical Journal* 2006, **90**, 2404-2413). AFM has been used extensively to characterize biological samples because it can be routinely performed in natural fluid environments, which is a clear advantage over vacuum conditions imposed by the TEM. A key feature of the work was the ability to correlate membrane topographic features with the locations of fluorescently tagged proteins and lipids, through simultaneous acquisition of AFM and confocal fluorescence images.

Our results revealed the presence of distinct membrane features (raised domains) that have the ability to concentrate numerous membrane molecules, including cross-linked receptors, gangliosides and clathrin. The principal effect of cell activation is to cause the reorganization of membrane components into larger domains. Based on composition, we concluded that the raised domains seen by AFM correspond to the dark patches observed in TEM images of signaling domains that also localize the immunoreceptor FcεRI, at least 10 associated signaling molecules, and also molecules involved in coated pit assembly to dark regions of activated mast cell membrane. Thus we suggested that they represent areas that concentrate transmembrane and peripheral membrane proteins, and that their bulky cytoplasmic tails and associated binding partners contribute to the height. Finally, we showed by TEM that the cholesterol marker PFO preferentially binds darkened membranes and by AFM that cholesterol extraction causes a large reduction in height of the raised domains. These complementary results indicate that cholesterol

contributes significantly to the formation or stability of the raised domains. The mechanism is not known with certainty.

When present, a fibrous meshwork appeared to link adjacent raised domains, suggesting a role for the cortical cytoskeleton in organizing these prominent features of the plasma membrane landscape. The apparent relationship of the raised domains to the cytoskeleton is of particular interest. Elsewhere, previous diffusion experiments, such as fluorescence recovery after photobleaching data and single particle tracking data, have led to models that consider roles for cytoskeletal "fences" or "corrals" and anchored protein "pickets" in the temporary, dynamic confinement of membrane proteins and lipids and also in the formation of less mobile macromolecular complexes during signaling. However, particularly for particles linked to lipids, it has never been clear why interactions of the cytoskeleton with components of the inner leaflet of the membrane bilayer would regulate mobility in the outer leaflet of the bilayer. The AFM images acquired in our work showed cytoskeletal elements surrounding and connecting the raised domains. These images thus raise the possibility that the cortical cytoskeleton may determine the stability and characteristics of membrane domains, that in turn may determine the ability of proteins (and lipids) to access and escape from these specialized regions.

Overall the data suggested that signaling and endocytosis occur in mast cells from raised membrane regions that depend on cholesterol for their integrity and may be organized in specific relationship with the cortical cytoskeleton. AFM/fluorescence imaging of the inner membrane landscape revealed levels of topographical complexity that are not addressed either in the well-mixed lipid and protein models of membrane structure, or in progressively more complex models developed over the subsequent decades that incorporate concepts of compositional and functional heterogeneity within the membrane bilayer and between the membrane and the cytoskeleton.

Domain Structure in Model Membrane Bilayers Investigated by Simultaneous Atomic Force Microscopy and Fluorescence Imaging

A. R. Burns*

Biomolecular Materials and Interfaces Department, Sandia National Laboratories, MS 1413, Albuquerque, New Mexico 87185-1413

Received April 23, 2003. In Final Form: June 30, 2003

Simultaneous atomic force microscope (AFM) and submicron confocal fluorescence imaging of 1,2-dipalmitoyl-*sn*-glycero-3-phosphocholine (DPPC) lipid domain structures in 1,2-dioleoyl-*sn*-glycero-3-phosphocholine (DOPC) is presented. Lipids labeled by fluorescent probes either at the headgroups or tailgroups enable domain contrast in fluorescence imaging on the basis of partitioning between the gel (DPPC) and disordered liquid (DOPC) phases. However, correlation with AFM topographic information reveals that they do not always faithfully report exact gel domain size or shape. Furthermore, we find that the fluorescence contrast decreases significantly with domain size, such that small domains observed with AFM are not observed in fluorescence images despite adequate optical resolution. We attribute these effects in part to broadened partitioning of the probe lipids across the domain boundaries. Binding of fluorescent Alexa 488-conjugated cholera toxin B subunits to GM1 gangliosides in DPPC domains correlates well with AFM topographic information to the limit of optical resolution. However, it also may reveal the presence of dilute GM1 components in the fluid phase that have no topographic contrast. In all cases, the complete correlation of topographic and fluorescence images provides evidence that gel-phase domains occur across both leaflets of the bilayer.

1. Introduction

Supported lipid bilayers have been studied extensively as models for biological membranes[1−3] because of the ease by which they can be characterized by numerous techniques, particularly imaging microscopies. A 1−2 nm layer of water[1] between the solid support (usually glass or mica) and the lipids allows freedom of movement of both leaflets, thus preserving integrity of the bilayer as a membrane to a good approximation. Recently, there has been considerable activity in the study of distinct phase domains in multicomponent lipid bilayers and monolayers, both supported[4−12] and unsupported,[13−18] as models for "lipid rafts", believed to be important in cellular signaling processes.[19−24] Briefly, transmembrane and membrane-associated proteins involved in cellular signaling often have been shown to be components of densely packed, detergent-resistant domains of saturated lipids within the membrane.[19,21,22] The role of these "rafts" is thought to be one of binding or sequestering specific proteins for specialized functions within the membrane.[19−24] This association of proteins with lipid domains may in turn be mediated by much smaller "shells" of lipids surrounding the protein.[25] Thus, many studies of lipid domains in model systems have focused on phase separation within multicomponent lipid mixtures, on the basis of headgroup interactions and/or acyl chain structure, and the subsequent partitioning of protein-binding glycosphingolipids between the phases.

Domain structure in bilayer and monolayer assemblies has been characterized by numerous fluorescence microscopy methods including far-field[14,15,17,26] and near-field imaging,[27−29] fluorescence recovery after photobleaching,[10,13] and fluorescence quenching.[16,18] Indeed, these techniques have been useful for domain studies on cellular membranes as well.[19,30−34] Fluorescent labels are usually placed on specific lipids that subsequently partition

* To whom correspondence should be addressed. E-mail: aburns@sandia.gov.

(1) Johnson, S. J.; Bayerl, T. M.; McDermott, D. C.; Adam, G. W.; Rennie, A. R.; Thomas, R. K.; Sackmann, E. *Biophys. J.* **1991**, *59*, 289.
(2) Sackmann, E. *Science* **1996**, *271*, 43.
(3) Boxer, S. G. *Curr. Opin. Chem. Biol.* **2000**, *4*, 704.
(4) Dufrêne, Y.; Barger, W.; Green, J.-B.; Lee, G. *Langmuir* **1997**, *13*, 4779.
(5) Vié, V.; Mau, N.; Lesniewska, E.; Goudonnet, J.; Heitz, F.; Le Grimellec, C. *Langmuir* **1998**, *14*, 4574.
(6) Kramer, A.; Wintergalen, A.; Sieber, M.; Galla, H. J.; Amrein, M.; Guckenberger, R. *Biophys. J.* **2000**, *78*, 458.
(7) Yuan, C.; Johnston, L. J. *Biophys. J.* **2001**, *81*, 1059.
(8) Milhiet, P.-E.; Vié, V.; Giocondi, M.-C.; Le Grimellec, C. *Single Mol.* **2001**, *2*, 109.
(9) Dietrich, C.; Bagatolli, L. A.; Volovyk, Z. N.; Thompson, N. L.; Levi, M.; Jacobson, K.; Gratton, E. *Biophys. J.* **2001**, *80*, 1417.
(10) Dietrich, C.; Volovyk, Z. N.; Levi, M.; Thompson, N. L.; Jacobson, K. *Proc. Natl. Acad. Sci. U.S.A.* **2001**, *98*, 10642.
(11) Giocondi, M.-C.; Vié, V.; Lesniewska, E.; Milhiet, P.-E.; Zinke-Allmang, M.; Le Grimellec, C. *Langmuir* **2001**, *17*, 1653.
(12) Yuan, C.; Furlong, J.; Burgos, P.; Johnston, L. J. *Biophys. J.* **2002**, *82*, 2526.
(13) Almeida, P. F. F.; Vaz, W. L. C.; Thompson, T. E. *Biochemistry* **1992**, *31*, 7198.
(14) Korlach, J.; Schwille, P.; Webb, W. W.; Feigenson, G. W. *Proc. Natl. Acad. Sci. U.S.A.* **1999**, *96*, 8461.
(15) Bagatolli, L. A.; Gratton, E. *Biophys. J.* **2000**, *79*, 434.
(16) Wang, T.-Y.; Silvius, J. R. *Biophys. J.* **2000**, *79*, 1478.
(17) Samsonov, A. V.; Mihalyov, I.; Cohen, F. S. *Biophys. J.* **2001**, *81*, 1486.
(18) Wang, T.-Y.; Silvius, J. R. *Biophys. J.* **2003**, *84*, 367.
(19) Simons, K.; Ikonen, E. *Nature* **1997**, *387*, 569.
(20) Brown, R. E. *J. Cell Sci.* **1998**, *111*, 1.
(21) Harder, T.; Scheiffele, P.; Verkade, P.; Simons, K. *J. Cell Biol.* **1998**, *141*, 929.
(22) Brown, D. A.; London, E. *Annu. Rev. Cell Dev. Biol.* **1998**, *14*, 111.
(23) Jacobson, K.; Dietrich, C. *Trends Cell Biol.* **1999**, *9*, 87.
(24) Simons, K.; Ikonen, E. *Science* **2000**, *290*, 1721.
(25) Anderson, R.; Jacobson, K. *Science* **2002**, *296*, 1821.
(26) Radhakrishnan, A.; Anderson, T. G.; McConnell, H. M. *Proc. Natl. Acad. Sci. U.S.A.* **2000**, *97*, 12422.
(27) Hollars, C. W.; Dunn, R. C. *Biophys. J.* **1998**, *75*, 342.
(28) Vaccaro, L.; Schmid, E. L.; Ulrich, W.-P.; Vogel, H.; Duschl, C.; Marquis-Weible, F. *Langmuir* **2000**, *16*, 3427.
(29) Yuan, C.; Johnston, L. J. *J. Microsc.* **2002**, *205*, 136.
(30) Enderle, T.; Ha, T.; Ogletree, D. F.; Chemla, D. S.; Magowan, C.; Weiss, S. *Proc. Natl. Acad. Sci. U.S.A.* **1997**, *94*, 520.

10.1021/la030175x CCC: $25.00
Published on Web 08/21/2003

between the gel-phase (or liquid-ordered) raft domains and the liquid-disordered domains, although labeling of interacting proteins is also used. It is difficult to minimize the influence of the label on the lipid interaction with its neighbors; thus, the location of the label, on the headgroup or acyl chains, as well as acyl chain length,[18] can lead to significant differences in partitioning.

Atomic force microscopy (AFM) has been used to image organizational structure in supported lipid monolayers and the top leaflet of bilayers on the basis of topographic height differences between gel-phase and liquid-disordered domains.[4,5,7,8,12] The origin of this height difference most likely arises because the "taller" gel-phase domains of saturated acyl chains are more tightly packed relative to liquid disordered domains (usually lipids with unsaturated acyl chains); thus, they occupy a smaller area per molecule and are oriented more normal to the substrate.[4] Microdomains of glycosphingolipids, such as GM1, have been resolved on the basis of their large headgroups.[5,7,8,12] Like fluorescence imaging, AFM can be routinely performed with the model membranes in fluid environments, thus allowing lipid mobility and full interaction with solutes such as proteins. It has also been well-established that AFM can provide undistorted molecular-scale lateral (<2 nm) and vertical (<0.1 nm) resolution of compliant membrane structures, due in large part to sensitive force feedback detection (<1 nN) and sharp probes (<20 nm tip radius).[35−37] As with all scanning probes, AFM is primarily useful for imaging relatively "static" features that are not rapidly diffusing or changing shape.

The ability to correlate information gathered from fluorescence imaging on supported membranes in a fluid environment with detailed lateral structures mapped out with AFM would be highly advantageous. In a step toward this goal, the utility of performing simultaneous AFM and submicron confocal fluorescence imaging is demonstrated on lipid bilayers consisting of 1,2-dipalmitoyl-*sn*-glycero-3-phosphocholine (DPPC) gel-phase domains in a 1,2-dioleoyl-*sn*-glycero-3-phosphocholine (DOPC) liquid phase. It is shown that since the fluorescent labels are subject to partitioning between the gel (DPPC) and disordered (DOPC) lipid phases, they do not always faithfully report exact gel domain size or shape. Furthermore, the fluorescence contrast decreases significantly with domain size, such that small domains observed with AFM are not observed in fluorescence images despite adequate optical resolution. Fluorescent markers do, however, reveal the presence of dilute components in the fluid phase that have no topographic contrast.

2. Materials and Methods

2.1. Lipids and Protein. 1,2-Dipalmitoyl-*sn*-glycero-3-phosphocholine, 1,2-dioleoyl-*sn*-glycero-3-phosphocholine, and GM1 ovine brain ganglioside were purchased from Avanti Polar Lipids and used without further purification. *N*-(4,4-Difluoro-5,7-dimethyl-4-bora-3*a*,4*a*-diaza-*s*-indacene-3-propionyl)-1,2-dipalmitoyl-*sn*-glycero-3-phosphoethanolamine (BODIPY-DPPE, also known as BODIPY-DHPE), *N*-(4,4-difluoro-5,7-dimethyl-4-bora-3*a*,4*a*-diaza-*s*-indacene-3-propionyl)-C5-ganglioside GM1 (BODIPY-C5-GM1), and Alexa 488-conjugated cholera toxin B subunit (Alexa 488-CTX-B) were purchased from Molecular Probes and used without purification unless otherwise indicated.

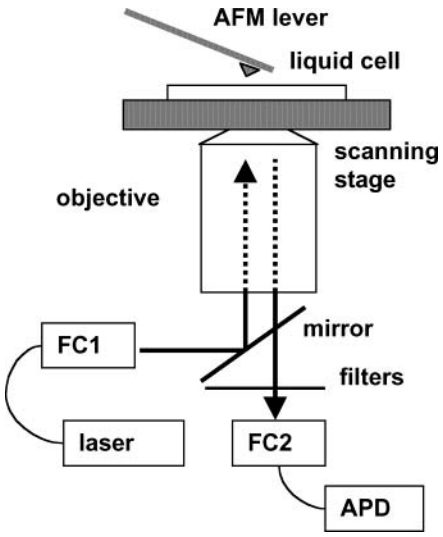

Figure 1. Schematic (not to scale) of experimental apparatus for acquiring AFM and fluorescence images. See text for details. FC1 and FC2 are fiber couplers for excitation light and fluorescence emission, respectively. APD is an avalanche photodiode. The scanning stage is mounted on an inverted microscope stage (not shown).

2.2. Supported Bilayers. Lipid bilayers are formed on glass coverslips by the method of vesicle fusion.[2,3] Single unilamellar vesicles are prepared by first dissolving the lipids in chloroform, followed by rotary evaporation of the solvent and drying for over 12 h under high vacuum. The lipids are resuspended by adding phosphate-buffered saline (PBS) buffer (100 mM NaCl, 40 mM sodium phosphate, pH 7.4) and vortexing, followed by degassing with nitrogen. The mixtures are tip-sonicated for 4 min cycles over 20 min while being cooled with an ice bath. The resulting vesicle suspensions are centrifuged at 15000 rpm, with the supernatant filtered through a 0.2 μm syringe filter. Dynamic light scattering characterization (Protein Solutions) usually indicates vesicles diameters are in the range of 50−100 nm.

Glass coverslips (0.13−0.17 mm thickness) are cleaned in (7:3) H_2SO_4/H_2O_2, (*caution*: *this is potentially explosive when reacting with organics*), rinsed thoroughly in distilled and ultrapure water (Barnstead Nanopure), and stored under ultrapure water (18 MΩ·cm). Just prior to use, the coverslips are dried under a stream of pure, dry nitrogen and mounted in a Leiden coverslip dish (Harvard Apparatus). The ∼3 mM vesicle solution is pipetted onto the coverslip and diluted (1:5) with imaging PBS buffer (150 mM NaCl, 50 mM sodium phosphate, 1. 5 mM NaN_3, pH 7.4). After 2 h of incubation at 60 °C, followed by cooling to room temperature, the lipid bilayer is rinsed thoroughly with imaging PBS buffer and mounted on the microscope. When required, incubation of the lipid bilayers with Alexa 488-CTX-B stock solution (10 μg/mL, in imaging PBS buffer) is performed for 1−2 min, followed by thorough rinsing with imaging PBS buffer. Prior to use, the stock solution was passed through chromatography columns (Sephadex G25 or Bio Rad Micro Bio Spin 6) to reduce the amount of unconjugated Alexa 488.

2.3. AFM and Fluorescence Microscopy. The experimental apparatus for obtaining simultaneous AFM and fluorescence images of lipid bilayers is shown schematically (not to scale) in Figure 1. The instrument is based on an inverted microscope (Olympus IX-70) platform modified to accommodate an AFM scan head (Digital Instruments Bioscope G scanner). The microscope is mounted on a vibration isolation air table that is also acoustically- and light-isolated. The liquid cell (coverslip dish) is mounted on a flat-plate *XY* scanner (Nanonics) that allows full optical access below and AFM access above the sample. Excitation light from a continuous 488 nm Ar^+ laser (on a separate table) is coupled into a single-mode optical fiber that ports the light to the microscope table and also serves as a spatial filter. A fiber coupler (FC1 in Figure 1) then forms a collimated Gaussian beam that reflects off a dichroic mirror (Chroma Q495LP) and

(31) Hwang, J.; Gheber, L. A.; Margolis, L.; Edidin, M. *Biophys. J.* **1998**, *74*, 2184.
(32) Varma, R.; Mayor, S. *Nature* **1998**, *394*, 798.
(33) Kenworthy, A. K.; Petranova, N.; Edidin, M. *Mol. Biol. Cell* **2000**, *11*, 1645.
(34) Schütz, G. J.; Sonnleitner, M.; Schindler, H. *J. Fluoresc.* **2001**, *11*, 177.
(35) Müller, D. J.; Fotiadis, D.; Engel, A. *FEBS Lett.* **1998**, *430*, 105.
(36) Müller, D. J.; Heymann, J. B.; Oesterhelt, F.; Möller, C.; Gaub, H.; Büldt, G.; Engel, A. *Biochim. Biophys. Acta* **2000**, *1460*, 27.
(37) Czajkowsky, D. M.; Shao, Z. *FEBS Lett.* **1998**, *430*, 51.

fills the back plane of a 100× (1.3 NA) oil immersion objective. The objective focuses the light (<2 μW) to a 250−300 nm spot size spatially coincident on the sample with the pyramidal tip on the end of the AFM cantilever, as can been seen through the microscope eyepiece. This alignment remains fixed as the sample is scanned. Epi-fluorscence emission is collected by the same objective and passes through the dichroic mirror, through two notch filters (488 and 670 nm, Kaiser), and through a 500−580 nm band-pass filter (Chroma HQ 540/80). The fluorescence is then spatially filtered in a confocal manner by coupling (FC2 in Figure 1) into a 50 μm diameter core multimode fiber connected to an avalanche photodiode detector (EG&G SPCM-AQR).

A single controller (RHK Technology) is used for sample scanning, AFM feedback, and photon counting of the fluorescence, thus providing simultaneous topographic and fluorescence images. Fluorescence background count rates for blank substrates were less than 1 kHz. A slight nanometer-scale offset between the two images is possible due the alignment of the laser focus on the AFM lever. All the AFM data presented here were acquired with levers (Olympus TR400-PSA; nominal force constant of 0.08 N/M) in contact mode under a feedback load ≤ 0.2 nN. Force calibration was checked with the thermal power spectrum method.[38] The *XY* scanner plate was calibrated with a 463 nm square grid grating (Ted Pella, Inc.), and the AFM head was calibrated in *Z* with known 25.5 nm steps (TGZ01, NT-MDT Mikromasch).

3. Results and Discussion

Lipid bilayers were created from a 3:1 molar mixture of DOPC/DPPC and various fluorescent probes. In all cases, the vesicle fusion process, which occurred above the gel−fluid transition temperature of DPPC (41 °C), produced bilayers without apparent defects. Due to the allotment of least 1 h for temperature equilibration of the cantilevers in the coverslip dish, there was ample time for the stabilization of the gel/fluid phases.[11] Thus, the images shown below were static for the period of several hours.

In Figure 2 are shown 3.0 μm AFM and fluorescence images acquired simultaneously of a DOPC/DPPC (3:1) bilayer with 0.5% BODIPY-DPPE. The gel domains of DPPC are readily observed in the AFM images (Figure 2A) on the basis of the 1.1 ± 0.2 nm height above the DOPC fluid phase, consistent with previous results.[4,5,7,8,12] The DPPC domains have irregular shapes and a size distribution ranging from 10 nm to >1 μm. In the corresponding fluorescence image (Figure 2B), the domains are darker than the surrounding DOPC, thus revealing that the BODIPY-DPPE is excluded from the DPPC domains. Due in part to the 300 nm limit in confocal optical resolution, the domain boundaries are blurred in the fluorescence image and thus lack the detail observed in the topographic image. Also, by having both AFM and fluorescence images, one can readily observe that in the fluorescence image larger domains are darker that the smaller ones.

The BODIPY label is situated on the DPPE headgroup, thus leaving the saturated acyl chains unperturbed relative to the DOPC/DPPC matrix. Since BODIPY-DPPE and DPPC have identical saturated acyl chains, it is surprising that the probe lipid tends to be excluded from the tightly packed DPPC domains. It is thus perhaps due to headgroup interactions that it goes into the DOPC fluid phase. Similar behavior was observed for headgroup-labeled DPPE probes in Langmuir−Blodgett monolayers.[9,10,26] The BODIPY-DPPE is not completely excluded from the gel domains, however, as can be seen from the fluorescence intensity profile in Figure 2C. The lowest count rates, corresponding to the darkest regions, still exceed the background count rate of 1 kHz by several orders of magnitude. For the most part, the gradual slope of the fluorescence line profile relative to the sharp domain boundaries delineated in the topograph line profile (also shown in Figure 2C) is due to the limited (300 nm) optical resolution. However, there is a small, additional broadening that indicates that the BODIPY-DPPE partitioning is not sharp across the boundary. This gradient of the BODIPY-DPPE concentration associated with the domain boundary is more obvious in Figure 3, where AFM and fluorescence images are shown for a very large DPPC domain in the same sample.

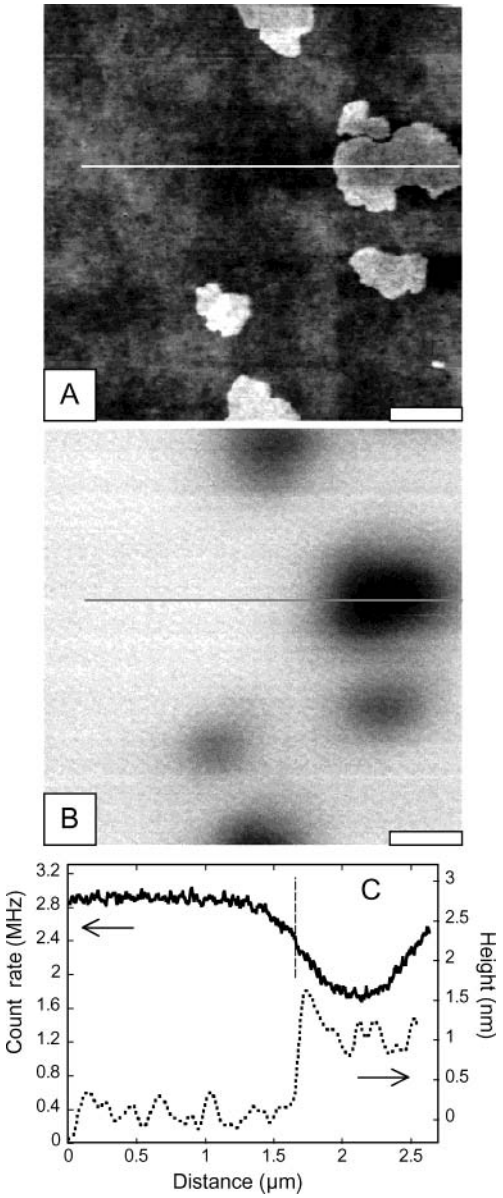

Figure 2. 3.0 μm scan featuring topographic (A) and fluorescence (B) images of a 3:1 DOPC/DPPC bilayer, with 0.5% BODIPY-DPPE, on glass (scale bar = 500 nm). The height of the DPPC domains in A is 1.1 ± 0.2 nm. In the fluorescence image (B), the dark regions are due to the exclusion of the headgroup-labeled BODIPY-DPPE from the DPPC domains. The smaller domains are not as dark as the largest, indicating less exclusion. In C, a fluorescence line profile (solid) and corresponding topographic line profile (dotted) are plotted for the largest domain. The left boundary of the domain is marked by the dashed line.

The fluorescent line profile in Figure 3C clearly indicates that the relative exclusion of the BODIPY-DPPE from the large DPPC domain increases with distance from the domain boundary to the center of the domain. For the

(38) Hutter, J. L.; Bechhoefer, J. *Rev. Sci. Instrum.* **1993**, *64*, 1868.

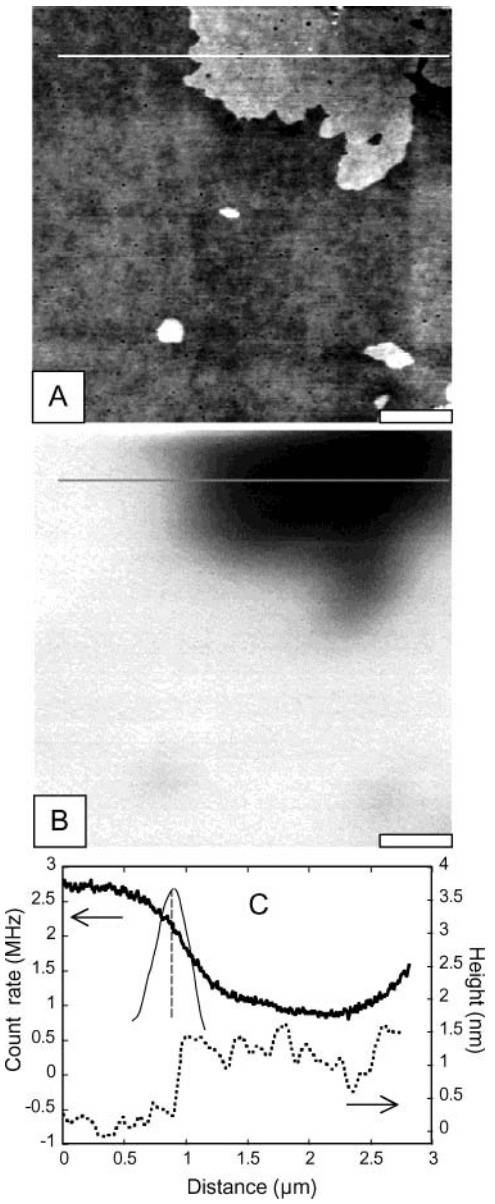

Figure 3. 3.0 μm scan featuring topographic (A) and fluorescence (B) images of a 3:1 DOPC/DPPC bilayer, with 0.5% BODIPY-DPPE, on glass (scale bar = 500 nm). The height of the DPPC domains in A is 1.1 ± 0.2 nm. The large domain is likely formed by coalescence of smaller domains, as evidenced by residual pockets of DOPC. In the fluorescence image (B), the dark region is due to the exclusion of the headgroup-labeled BODIPY-DPPE from the DPPC domains. It does not appear to be excluded from the small domains, although optical resolution is limiting detection of the smallest. In C, a fluorescence line profile (solid) and corresponding topographic line profile (dotted) are plotted for the large domain. The left boundary of the domain is marked by the dashed line. Overlaid on this dashed line is a diffraction-limited (300 nm) line profile (thin solid) to show that the fluorescence line profile is considerably broadened beyond the diffraction limit.

sake of comparison with previous results, one can estimate a maximum relative partition coefficient $R = (I_G/(I_G+I_L))$, where I_G is the intensity at the center of the domain and I_L is the intensity well outside the domain. For Figure 3C, $R \cong 0.25$, whereas, for Figure 2C, $R \cong 0.37$. For fluorescein headgroup-labeled DPPE, a coefficient $R = 0.14$ has been measured for partitioning into large (>1.0 μm) sphingomyelin−chloesterol domains in DOPC.[10] Thus, the R value for Figure 3C is comparable, despite the change in lipids and probe. The larger R value for the smaller domain in Figure 2C points to an important aspect of the simultaneous AFM and fluorescence images presented in Figures 2 and 3: the smallest domains exhibit the weakest fluorescence contrast, not only because they are more difficult to optically resolve but also because the relative partition coefficient of the probe lipid is approaching 0.5 (i.e., uniform coverage). The apparent gradient in the BODIPY-DPPE probe concentration across the domain boundaries also has the potential to mask irregular domain shapes (possibly indicating solid-phase domains[39]) and make them appear more circular (indicating more fluidlike domains). Furthermore, a very important question arises from these observations: is the boundary between the DOPC fluid-phase region and DPPC gel-phase region really as sharp as that indicated by the AFM topographic data? A slight mixing of the two components across the domain boundary would help to explain the partitoning results and also make possible an initial decrease of the BODIPY-DPPE concentration on the "DOPC side" of the topographically defined boundary.

The glycosphingolipid GM1 has been shown in several fluorescence[9,10,17,18,26] and AFM studies[5,7,8,12] to partition into the gel-phase domains. It is even thought to be immiscible in DOPC.[26] However, when the acyl chains are modified with a fluorescent probe, as is the case with BODIPY-C5-GM1, one can see from the 6.0 μm images presented in Figure 4 that the tailgroup-labeled GM1 is predominantly excluded from the DPPC gel-phase and resides in the DOPC matrix. This observation is consistent with previous bilayer domain studies using tailgroup-labeled sphingolipids.[16,17] The exclusion of the tailgroup-labeled BODIPY-C5-GM1 from the gel phase is most likely due to the larger molecular area induced by steric interference between the probe and the longer acyl chains.[18] From the fluorescence line profile (Figure 4C), the BODIPY-C5-GM1 partition coefficient $R \cong 0.25$ at the center of the domain, where it is fairly flat over at least 1.5 μm. Just as discussed above with the headgroup-labeled DPPE, we see in Figure 4B,C a more gradual partitioning of the tailgroup-labeled GM1 between the two phases than is dictated by the phase boundary or the 300 nm optical resolution. Finally, as expected for AFM imaging in a fluid phase, the large GM1 headgroups are completely unresolved and no aggregation of the GM1 is observed in the DOPC regions. However, the DPPC domains in Figure 4A are now 0.8 ± 0.1 nm higher than the surrounding DOPC, a slightly smaller difference than that (1.1 ± 0.2 nm) observed in Figures 2 and 3 in the absence of GM1, and which may reflect the presence of GM1.

An important issue that is mentioned in numerous studies of lateral structure in model lipid bilayers is the superposition of domains between the bilayer leaflets; i.e., do the domains span both leaflets of the bilayer? Much evidence has been presented, particularly via fluorescence techniques,[9,13,14,17] that this is indeed the case. The evidence resides in that no overlapping of different-sized domains is observed, nor are there "gray" features that derive from emission from only one leaflet and thus are half the intensity of emission from bilayer domains. These observations are also supported by the fluorescence images obtained in the present work. However, as discussed above, one notes that domains in Figures 2 and 3 become less and less dark with shrinking size due in part to the diminished exclusion of the probe lipid. Thus, the gray criteria would lead to erroneous conclusions for small domains (<1 μm) relative to large domains (>1 μm). The

(39) Veatch, S. L.; Keller, S. L. *Phys. Rev. Lett.* **2002**, *89*, 268101.

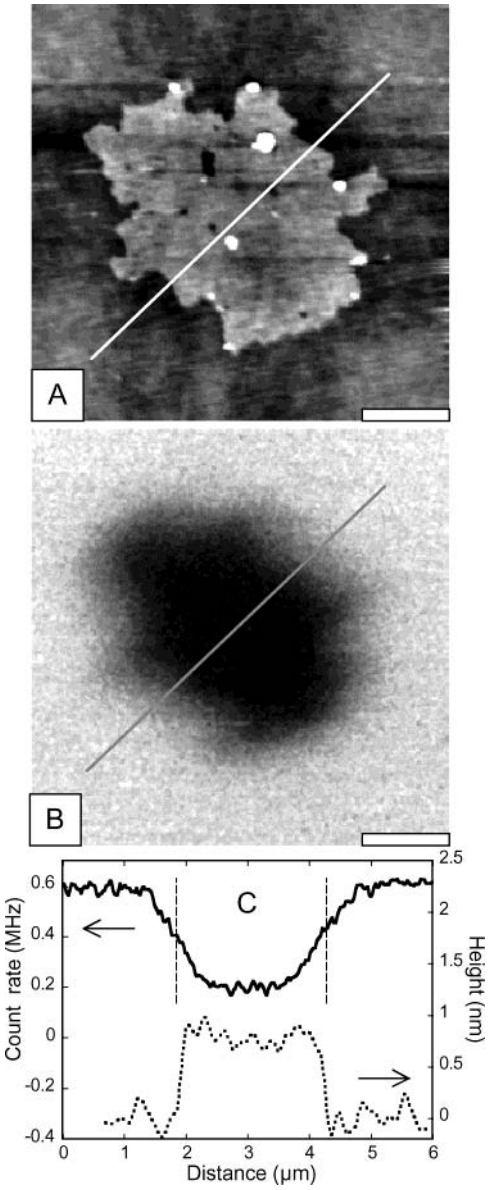

Figure 4. 6.0 μm scan featuring topographic (A) and fluorescence (B) images of a 3:1 DOPC/DPPC bilayer, with 0.25% BODIPY-GM1, on glass (scale bar = 1.0 μm). The height of the DPPC domain in A is 0.8 ± 0.1 nm. In the fluorescence image (B), the dark region is due to the exclusion of the tailgroup-labeled GM1 from the DPPC domains. In C, a fluorescence line profile (solid) and corresponding topographic line profile (dotted) are plotted. The left and right boundary of the domain is marked by the dashed lines.

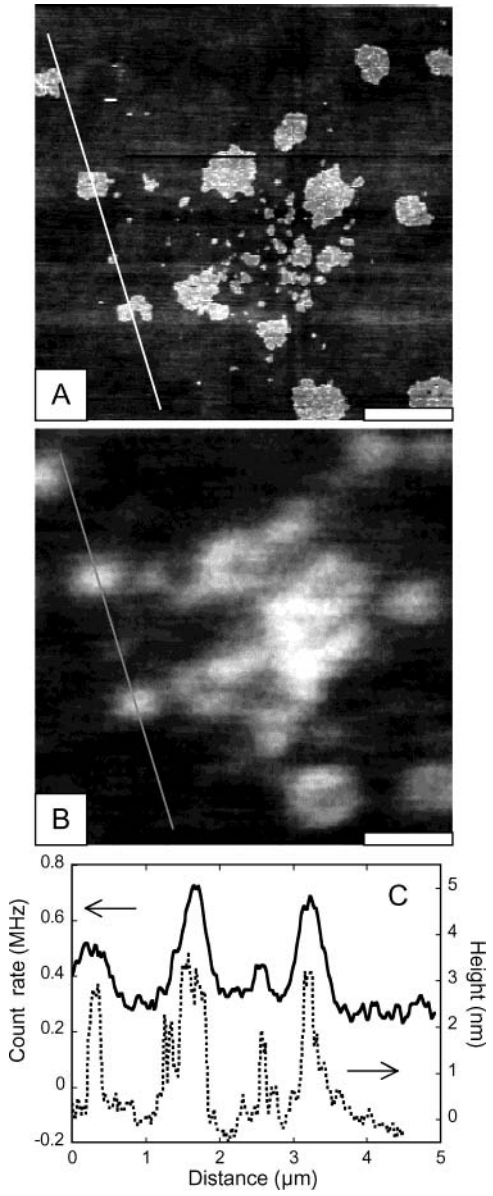

Figure 5. 5.0 μm scan featuring topographic (A) and fluorescence (B) images of a 3:1 DOPC/DPPC bilayer, with Alexa 488-CTX-B bound to 1.0% unlabeled GM1, on glass (scale bar = 1.0 μm). The combined height of the DPPC domains and bound CTX-B in A is 3.2 ± 0.3 nm. In the fluorescence image (B), the bright regions are due to the Alexa 488-labeled CTX-B bound to the DPPC domains. In C, a fluorescence line profile (solid) and corresponding topographic line profile (dotted) are plotted. The fluorescence line shapes of the two prominent features are diffraction-limited (fwhm ≅ 300 nm).

question of leaflet superposition of domains is more easily verified here than in previous studies because there is always a correlation between the AFM and fluorescence images. For each domain in the fluorescence there is a corresponding feature in the AFM topography. If there was poor registry between leaflets, then one would expect to see light or dark regions in the fluorescence images without topographic correlation.

Alexa 488-CTX-B binds to GM1 receptors and thus is an effective way to detect or "stain" unlabeled GM1 in the upper leaflet.[9,10,26] In Figure 5, the simultaneous AFM and fluorescence images are shown for a (3:1) DOPC/DPPC bilayer containing 1% GM1 that is subsequently incubated with Alexa 488-CTX-B. As expected from previous results,[9,10,26] the unlabeled GM1 is now readily incorporated into the DPPC domains seen in the AFM image (Figure 5A) and which appear bright in the fluorescence image (Figure 5B) due to the presence of GM1-bound Alexa 488-CTX-B. Due to the toxin binding to GM1, the DPPC domains in the AFM image now have a height of 3.2 ± 0.3 nm relative to the DOPC matrix. High-resolution images (not shown) of the DPPC domains reveal a uniform coverage of close-packed 7 nm features that correspond to CTX-B pentamers.[37] The fluorescence image shown in Figure 5B has distinct features not seen in the other data (Figures 2−4). The domains are uniformly bright and do not exhibit a fading toward the domain boundary. Thus, the small domains (<1 μm) are as bright as the larger domains, and the sharpness of the fluorescence features as seen in the line profile (Figure 5C) is limited only by the 300 nm optical resolution of the domain boundaries and not by partitioning of the GM1 to the DOPC fluid phase. Thus, it appears that the unlabeled GM1 is

predominantly restricted to the DPPC gel phase and is uniformly distributed in it. However, there is a much larger than expected fluorescence background in the liquid DOPC phase. It may be attributed in part to unconjugated Alexa 488 probe, although the Alexa 488-CTX-B stock solution was passed through separation columns in an attempt to remove unconjugated probe. The background may also be attributed to a small component of the GM1 lipids (purified from ovine brain) that have acyl chains that could be excluded from the gel phase. Further studies on other lipid mixtures, such as DOPC/sphingomyelin/cholesterol,[10] where GM1 was shown to have a partition factor $R \cong 0.95$ for the gel-phase, are required before a conclusion can be drawn. In any case, an important point to note here is that fluorescence data have the potential to reveal the presence of GM1 in the fluid phase that would not be ordinarily detected by AFM.

4. Conclusions

Independent fluorescence and AFM imaging methods have been successfully used in the past to investigate domain formation in multicomponent lipid bilayers. It has been demonstrated here, for 3:1 DOPC/DPPC bilayers supported on glass, that the simultaneous acquisition of fluorescence and AFM topographic information provides insights on lateral organization that either technique alone would not necessarily be able to provide. Well-defined gel-phase DPPC domains with irregular shapes and sizes ranging from 10 nm up to several micrometers were observed in AFM images on the basis of the ~1 nm height difference above the surrounding DOPC fluid-phase. In the fluorescence images, those same (resolvable) domains were observed by the selective partitioning of probe-labeled lipids for the liquid phase.

Correlation between the two sets of images revealed that the fluorescent probe lipid partitioning was not uniform across the domains, thus potentially distorting domain size and shape beyond that imposed by optical resolution. Factors that govern probe lipid partitioning across domain boundaries need to be studied in more detail. Models that incorporate both chemical and physical factors that not only lead to domain formation but also relative partitioning of tailgroup- and headgroup-labeled probes are required. This is complicated by the unknown lipid composition at these boundaries, despite the abrupt height difference in the bilayer topography. A more precise understanding of the topographical height difference between gel and fluid domains is also necessary in order to understand the multicomponent composition at the domain boundaries.

The results presented here also possibly indicate that the glycosphingolipid GM1 may not reside exclusively in the densely packed gel-phase domains as could be construed from AFM, but may have some finite concentration in the fluid phase as detected by fluorescence from bound, labeled protein. Future studies of lateral structure and signaling processes in model membranes and harvested biological membranes will surely benefit from combined techniques such as that presented here. Moreover, this work provides a basis and motivation for improvements in optical resolution provided by near-field enhanced fluorescence excitation at metallic AFM probe tips.[40,41]

Acknowledgment. The author is indebted to Tina Huber for preparation of lipid vesicles, Jennifer Gaudioso for column chromatography, and Peter Chen for substrate cleaning. Critical reading of the manuscript by Mark Stevens is also gratefully acknowledged. This research was supported in part by the Division of Materials Science and Engineering, Office of Basic Energy Sciences, U.S. Department of Energy. Sandia is a multiprogram laboratory operated by Sandia Corporation, a Lockheed Martin Company, for the U.S. Department of Energy under Contract DE-AC04-94AL85000.

LA030175X

(40) Sánchez, E. J.; Novotny, L.; Xie, X. S. *Phys. Rev. Lett.* **1999**, *82*, 4014.

(41) Yang, T. J.; Lessard, G. A.; Quake, S. R. *Appl. Phys. Lett.* **2000**, *76*, 378.

Local Mobility in Lipid Domains of Supported Bilayers Characterized by Atomic Force Microscopy and Fluorescence Correlation Spectroscopy

A. R. Burns,* D. J. Frankel,* and T. Buranda†
*Biomolecular Materials and Interfaces Department, MS 1413 Sandia National Laboratories, Albuquerque, New Mexico 87185; and †Department of Pathology, University of New Mexico School of Medicine, Albuquerque, New Mexico

ABSTRACT Fluorescence correlation spectroscopy (FCS) is used to examine mobility of labeled probes at specific sites in supported bilayers consisting of 1,2-dipalmitoyl-*sn*-glycero-3-phosphocholine (DPPC) lipid domains in 1,2-dioleoyl-*sn*-glycero-3-phosphocholine (DOPC). Those sites are mapped beforehand with simultaneous atomic force microscopy and submicron confocal fluorescence imaging, allowing characterization of probe partitioning between gel DPPC and disordered liquid DOPC domains with corresponding topography of domain structure. We thus examine the relative partitioning and mobility in gel and disordered liquid phases for headgroup- and tailgroup-labeled GM1 ganglioside probes and for headgroup- and tailgroup-labeled phospholipid probes. For the GM1 probes, large differences in mobility between fluid and gel domains are observed; whereas unexpected mobility is observed in submicron gel domains for the phospholipid probes. We attribute the latter to domain heterogeneities that could be induced by the probe. Furthermore, fits to the FCS data for the phospholipid probes in the DOPC fluid phase require two components (fast and slow). Although proximity to the glass substrate may be a factor, local distortion of the probe by the fluorophore could also be important. Overall, we observe nonideal aspects of phospholipid probe mobility and partitioning that may not be restricted to supported bilayers.

INTRODUCTION

The lateral organization and dynamics of lipids and proteins in membranes is critical to many cellular processes. Thus there has been considerable interest in the study of membrane microdomains (''lipid rafts'') to determine their size, location, and function in membrane organization (1–3). Studies of domains in cellular membranes have relied heavily on fluorescence-based imaging of protein colocalization and lipid structure (4–6) and fluorescence-based dynamical studies of lipid probes and labeled proteins. Concerning dynamics, it is widely held that translational diffusion rates reflect not only the intrinsic mobility of membrane constituents but also the local structure of the membrane. Thus we have seen the application of a variety of techniques that offer considerable insight into diffusion processes in cellular membranes at various length scales. These include fluorescence recovery after photobleaching (FRAP) (7,8), single particle tracking (SPT) (7,9,10), and fluorescence correlation spectroscopy (FCS). Applications of FCS to diffusion in membranes have been discussed comprehensively in the literature (11–15). Since the sensitivity of time-dependent statistical analysis of fluorescence intensity in FCS scales inversely with detection volume and probe concentration, it is an excellent tool to complement low-light-level confocal fluorescence imaging of membranes.

Both fluorescence-based imaging and dynamics have also been essential to the analysis of the structure of lipid domains and component mobility in model membranes. Model membrane studies offer the ability to characterize phase separation, due to headgroup interactions and/or acyl chain structure, of gel or liquid-ordered domains (''rafts'') within multicomponent lipid mixtures, on the basis of subsequent partitioning of lipid probes or protein-binding glycosphingolipids between the phases (16–19). By partitioning, we refer to the process by which probes go preferentially into one domain but can be observed in both. It has been shown using FCS (20,21), FRAP (22,23), and SPT (24,25) that the two-dimensional lateral diffusion coefficient of most probes is strongly dependent on the lipid packing of the domains: $\sim 1\text{–}10 \times 10^{-8}$ cm^2/s in liquid-disordered phases to essentially immobile ($<10^{-11}$ cm^2/s) in gel phases.

Since dynamical processes are dependent on the local membrane structure as well as local molecular interactions, it would be advantageous to directly correlate dynamics information with detailed lateral dimensions and topography mapped out with atomic force microscopy (AFM). AFM has been successfully used to image domain structure in supported lipid monolayers and bilayers in fluid environments on the basis of topographic height differences between gel-phase, liquid-ordered, and liquid-disordered domains (23,26–28). Recently, simultaneous AFM and confocal fluorescence imaging was used to examine the partitioning of lipid probes between fluid and gel domain boundaries mapped with 1 nm lateral resolution (28). We now present FCS measurements of diffusion coefficients of lipid and glycolipid probes at precisely defined locations on supported bilayers mapped out with the same technique. The resolution is limited only by the spot size (~400 nm) of the laser beam on the sample. Of particular interest is the boundary region between domains. Also, it has been shown that the location of the fluorescent probe (e.g., headgroup versus tailgroup) on the lipid molecule has significant impact on partitioning between domains (18,19,28). Since partitioning and lateral diffusion are both

Submitted January 28, 2005, and accepted for publication April 29, 2005.
Address reprint requests to Alan R. Burns, E-Mail: aburns@sandia.gov.

0006-3495/05/08/1081/13 $2.00
doi: 10.1529/biophysj.105.060327

expected to be sensitive to local molecular interactions, it is of interest to determine if the location of the fluorescent probe influences the lateral diffusion as well. Thus, we examine the relative partitioning and diffusion coefficients in gel (DPPC) and disordered liquid (DOPC) phases and boundary regions for both headgroup- and tailgroup-labeled GM1 ganglioside as well as for headgroup- and tailgroup-labeled phospholipid analogs of DPPC. Since GM1 selectively binds cholera toxin B (CTX-B) fragments, we are also able to examine the effects of protein binding on GM1 mobility in the fluid DOPC phase.

Numerous studies of supported bilayers in fluid environments have shown that domain structure and freedom of movement of lipid components are, for the most part, preserved relative to unsupported membranes (22,23,29–32). This behavior is attributed to a 1–2 nm water layer that decouples the bilayer from the solid support and allows ''lateral'' lipid-lipid and ''vertical'' leaflet-leaflet interactions to dominate (33–35). Substrate effects have been reported, however, and include slower diffusion rates for probes proximal to the substrate (36) and altered phase behavior (37,38). The latter may be due to unrelieved stresses at domain boundaries created during bilayer formation and/or temperature cycling (39). Our results do indicate local heterogeneities in gel domain structure and a slow mobility component in the phospholipid probes. However, it is not clear whether those can be attributed to substrate effects or defects induced by the probes.

MATERIALS AND METHODS

Lipids and proteins

1,2-dipalmitoyl-*sn*-glycero-3-phosphocholine (DPPC), 1,2-dioleoyl-*sn*-glycero-3-phosphocholine (DOPC), and GM1 ovine brain ganglioside (GM1) were purchased from Avanti Polar Lipids (Alabaster, AL) and used without further purification. *N*-(4,4-difluoro-5,7-dimethyl-4-bora-3a,4a-diaza-s-indacene-3-propionyl)-1,2-dipalmitoyl-*sn*-glycero-3-phosphoethanolamine (BODIPY-DPPE, also known as BODIPY-DHPE), 2-(4,4-difluoro-5,7-dimethyl-4-bora-3a,4a-diaza-s-indacene-3-dodecanoyl)-1-hexadecanoyl-*sn*-glycero-3-phosphocholine (BODIPY-C12-DHPC), *N*-(4,4-difluoro-5,7-dimethyl-4-bora-3a,4a-diaza-s-indacene-3-propionyl)-C5-ganglioside GM1 (BODIPY-C5-GM1), biotinylated recombinant CTX-B subunit (B-CTX-B), Alexa Fluor 488 conjugated recombinant CTX-B subunit (Alexa-488 CTX-B), and Alexa Fluor 488 hydrazide were purchased from Molecular Probes (Eugene, OR) and used without purification unless otherwise indicated. Sodium meta-periodate and bovine brain asialoganglioside-GM1 were purchased from Sigma Chemical (St. Louis, MO) and used without further purification. It should be noted that the use of recombinant Alexa Fluor 488 CTX-B greatly reduces background emission that is found when non-recombinant CTX-B is used (28).

Synthesis of headgroup-labeled GM1 ganglioside

Alexa Fluor 488 hydrazide-conjugated GM1 (''Alexa-488 head-GM1'') was prepared by a modification of previous methods (40). Bovine brain asialoganglioside-GM1 (1 mg/mL) was suspended in 100 mM sodium acetate buffer (pH 5.5) with 1 mM sodium meta-periodate. The oxidation reaction was allowed to proceed for 30 min on ice. The suspension was then purified and concentrated by ultrafiltration in the same buffer using YM-30 Microcon centrifugal filters (Millipore, Bedford, MA), repeating five times to remove the sodium-meta periodate. A total of 10 mM Alexa Fluor 488 hydrazide was added to the oxidized GM1 and allowed to react with agitation for 2 h at room temperature. The fluorescent GM1 conjugates were freed of unreacted dye by using YM-30 Microcon centrifugal filters, repeating in PBS buffer, as described above, until the supernatant was optically clear. The labeled GM1 was dried under vacuum and stored as a powder under nitrogen at −20°C. Based on the mass of the GM1 before and after dye conjugation and absorption measurements, the Alexa:GM1 ratio was determined to be unity.

Supported bilayers

Lipid bilayers are formed on glass coverslips by the method of vesicle fusion (29,35). Small unilamellar vesicles are prepared by first dissolving the lipids in chloroform (Alexa-488 head-GM1 was dissolved in dimethyl sulfoxide), followed by rotary evaporation of the solvent and drying for over 12 h under high vacuum. The lipids are resuspended by adding phosphate-buffered saline (PBS) buffer (100 mM NaCl, 40 mM sodium phosphate, pH 7.4) and vortexing, followed by degassing with nitrogen. The lipid suspension was then subjected to a freeze thaw cycle followed by repeated extrusion (Northern Lipids, Vancouver, Canada) through 100 nm filter pores. Dynamic light scattering characterization (Protein Solutions, High Wycomb, UK) verified 100 nm vesicle diameters.

Glass coverslips (0.13–0.17 mm thickness) are cleaned in (7:3) H_2SO_4/H_2O_2 (caution: this is potentially explosive when reacting with organics), rinsed thoroughly in distilled water and ultrapure water (Barnstead Nanopure, Dubuque, IA), and stored under ultrapure water (18 MΩ-cm). Just before use, the coverslips are dried under a stream of pure, dry nitrogen and mounted in a Leiden coverslip dish (Harvard Apparatus, Holliston, MA). The ~3 mM vesicle solution is pipetted onto the coverslip and diluted (1:5) with imaging PBS buffer (150 mM NaCl, 50 mM sodium phosphate, 1. 5 mM NaN_3, pH 7.4). After 2 h of incubation at 60°C followed by 30 min of cooling to room temperature, the lipid bilayer is rinsed thoroughly with imaging PBS buffer and mounted on the microscope. When required, incubation of the lipid bilayers with Alexa 488-CTX-B or B-CTX-B stock solutions (10 μgr/ml, in imaging PBS buffer) is performed for 1–2 min, followed by thorough rinsing with imaging PBS buffer.

AFM and fluorescence microscopy

The experimental apparatus for obtaining simultaneous AFM and fluorescence images of lipid bilayers has been described previously and will be summarized here (28). An inverted microscope was modified to accommodate an AFM scan head and is mounted on an acoustically and light-baffled vibration isolation air table. The liquid cell (coverslip dish) is mounted on a flat-plate, closed-loop XY scanner (Mad City Labs, Madison, WI). Excitation light from a continuous 488 nm Ar^+ laser on a separate table is coupled into a single-mode optical fiber that forms a collimated Gaussian output beam. The beam reflects off a dichroic mirror and underfills (~80%) the back plane of a 100× (1.3 NA) oil immersion objective. The latter is used to optimize two-dimensional imaging and FCS work at the flat interface of the supported bilayer and the glass coverslip (41). The objective focuses the light (300 nW) to a diffraction-limited ~400 nm spot (see below) spatially coincident on the sample with the pyramidal tip on the end of the AFM cantilever, as can been seen through the microscope eyepiece. This alignment remains fixed as the sample is scanned. The optical resolution of the fluorescence image is optimized by minimizing the spot size on the sample. Epifluorescence emission passes through two notch filters (488 and 670 nm) and a 500–580 nm band-pass filter and is then spatially filtered by a 50-μm diameter core multimode fiber connected to an avalanche photodiode detector. Before a scan, the fluorescence signal from the minimized laser spot is optimized by the lateral and translational position of this 50-μm aperture.

Simultaneous AFM topographic and fluorescence images are acquired by a single controller for sample scanning, AFM feedback, and photon counting of the fluorescence. Closed-loop control of the XY scanner is performed automatically by separate electronics that are interfaced to the imaging controller. The XY scanner plate was calibrated with a 463 nm square grid grating (Ted Pella, Redding, CA), and the AFM head was calibrated in Z with known 25.5 nm steps (TGZ01, NT-MDT, Mikromasch USA, Portland, OR). Fluorescence background count rates for blank substrates were <1 KHz. A slight offset between the two images is possible due to the manual alignment of the laser focus on the AFM probe tip. All the AFM data presented here were acquired with cantilevers (Olympus TR400-PSA, Tokyo, Japan, nominal force constant of 0.08 N/M) in tapping mode.

Fluorescence correlation spectroscopy

FCS was performed with the AFM-fluorescence imaging apparatus discussed above in conjugation with a correlator (ALV-6010/160, Langen, Germany) interfaced to a separate computer using software supplied with the correlator (ALV Correlator Software Version V.3.1.12). Calibration of the laser spot size ($1/e^2$ Gaussian radius $= 0.22$ μm for 488 nm light) on the surface of the coverslip at the same power level (300 nW) and same optical pathway used for all imaging and FCS was determined by fitting the diffusion data acquired for a 10^{-7} M solution of rhodamine 6G in a coverslip dish to the value 2.8×10^{-6} cm^2/s (42). Precise control of the laser spot position on the sample was maintained by the closed-loop XY scanner, which eliminates drift and nonlinearities common to piezoceramic actuators used in AFM (43). The laser spot focus and the 50-μm multimode fiber spatial filter are optimized as discussed above for imaging. FCS data acquisition was performed as follows: 1), 256×256 pixel AFM and fluorescence images of supported bilayers were acquired and stored in memory; 2), the AFM cantilever was withdrawn from the sample to minimize light scattering (a precaution, not a problem); 3), the APD signal output was disconnected from the fluorescence imaging photon counter and connected directly to the correlator with an impedance-matched cable; 4), the fluorescence image was displayed and, with an image controller cursor, the position of the XY scanner was moved to a spot in the fluorescence image; and 5), FCS data was acquired for 100 seconds at that spot. The correlator also monitored the fluorescence count rate so that photobleaching could be detected if occurring. Steps 4 and 5 were repeated for many different spots in the fluorescence image. The raw FCS data were not averaged at one spot, but rather many spots were sampled and analyzed independently. Diffusion coefficients were then averaged, unless otherwise noted.

Analysis of FCS data for two-dimensional translational diffusion has been thoroughly discussed elsewhere (11–13) and will be briefly summarized here. Fluctuations $\delta F(t) = F(t) - \langle F(t)\rangle$ in the fluorescence intensity F are autocorrelated over discrete time intervals τ by the function $G(\tau)$:

$$G(\tau) = \langle \delta F(t)\delta F(t+\tau)\rangle / \langle F\rangle^2. \quad (1)$$

Brownian diffusion has a mean square displacement $\langle x^2\rangle = 4D\tau$, where D is the sought after diffusion coefficient. It can be shown that for fluorescence fluctuations due to two-dimensional diffusion of N molecules (11)

$$G(\tau) = \frac{1}{N}\sum_{j}\frac{Cj}{(1+\tau/\tau_{d,j})}, \quad (2)$$

where $\tau_{d,j} = w^2/4D_j$ is the average residence interval for molecular component j with fraction C_j within the confines of the Gaussian beam waist w. Other factors that may contribute to fluorescence fluctuations, such as single-triplet intersystem crossing (44), were found to be negligible for the dyes and timescales used in these experiments. For labeled probe molecules of one type undergoing unrestricted lateral diffusion, Eq. 2 reduces to a single component (D) fit. However, if sample heterogeneities exist, the data may exhibit two components, ''fast'' and ''slow'', with fractions C_{fast} and C_{slow} and diffusion coefficients D_{fast} and D_{slow}, respectively.

RESULTS AND DISCUSSION

Simultaneous AFM-fluorescence imaging of probe partitioning

In this section, we present simultaneous AFM-fluorescence images of bilayers (all 3:1 DOPC/DPPC) having various headgroup- and tailgroup-labeled GM1 and phospholipid analog fluorescent probes. The images are acquired under the same optical conditions that are subsequently used for the FCS experiments. Thus they not only provide information with regard to domain structure and probe partitioning but also serve as ''maps'' to guide the location of the FCS data acquisition. The probe concentrations are ~0.05% so that both imaging and FCS can be performed on the same sample in sequence. These low probe concentrations preclude precise quantitative partitioning analysis; thus only qualitative characterization is presented.

Since, as we discuss below, the presence of fluorophores can change the partitioning of lipids between liquid-disordered and gel domains, we begin by discussing simultaneous AFM-fluorescence images of bilayers that contain 0.5% unmodified GM1 that partitions strongly into the tightly packed DPPC gel domains (17,45). (We used 0.5% GM1 rather than 0.05% to make certain that a detectable amount is in the DOPC fluid phase for FCS discussed below.) In Fig. 1 *A*, it can be seen from the AFM topography that the DPPC forms (bright) irregularly shaped gel domains. The DPPC-DOPC height difference is 1.1 ± 0.2 nm, in agreement with other studies (26,46). When the unlabeled GM1 is stained by bound Alexa-488 CTX-B (17,45), the DPPC domains become 3.5 ± 0.2 nm higher that the DOPC fluid phase, in agreement with neutron reflectivity measurements (47). The Alexa-488 CTX-B is closely packed and uniformly covers the gel domains, indicating significant GM1 concentration. The GM1 preference for the gel domains is also clearly verified in the fluorescence image (Fig. 1 *B*), where the bright domains correlate with the AFM topography. The resolution

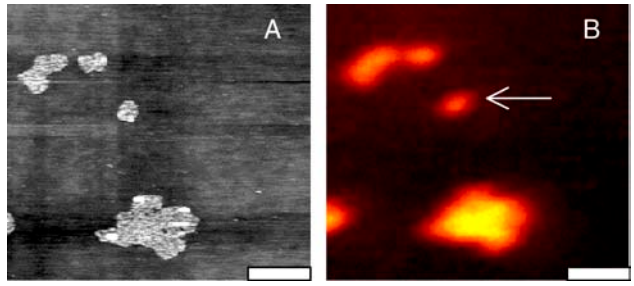

FIGURE 1 Simultaneous 5 μm AFM topography (*A*) and fluorescence (*B*) images (scale bar $= 1$ μm) of a 3:1 DOPC/DPPC with 0.5% GM1 bilayer on glass. The GM1 partitions to the DPPC domains where it binds Alexa-488 CTX-B. In the topography image, the bright DPPC domains usually are 1.1 ± 0.2 nm higher than the surrounding DOPC; in this case, having bound Alexa-488 CTX-B, they are 3.5 ± 0.2 nm higher. The fluorescence feature indicated by the arrow in *B* is resolved with a full width at half-maximum of ~300 nm.

of the smallest domains in the fluorescence image is at the diffraction limit (~300 nm full width half height), consistent with the FCS Gaussian beam waist calibration discussed in the previous section.

The partitioning in the 3:1 DOPC/DPPC domain structure of three probes used in this study differs considerably from that of unlabeled GM1. From the images shown in Fig. 2, one can see that the dark regions of the fluorescence images (indicating exclusion of the probe) correlate with the DPPC gel domains in the topography images (bright areas 1.1 ± 0.2 nm higher than DOPC). Thus the ''tailgroup-labeled GM1'' (BODIPY-C5-GM1) in Fig. 2, *A* and *B*, the ''tailgroup-labeled phospholipid'' (BODIPY-C12-DHPC) in Fig. 2, *E* and *F*, and the ''headgroup-labeled phospholipid'' (BODIPY-DHPE) in Fig. 2, *G* and *H*, are all excluded in varying degrees from the DPPC gel domains. The same probes, as well as similar probes using different fluorophores, have exhibited exclusion from ordered domains in other supported and unsupported monolayers (16,17,45,48) as well as bilayer vesicles (20,49). The presence of the fluorophore on saturated

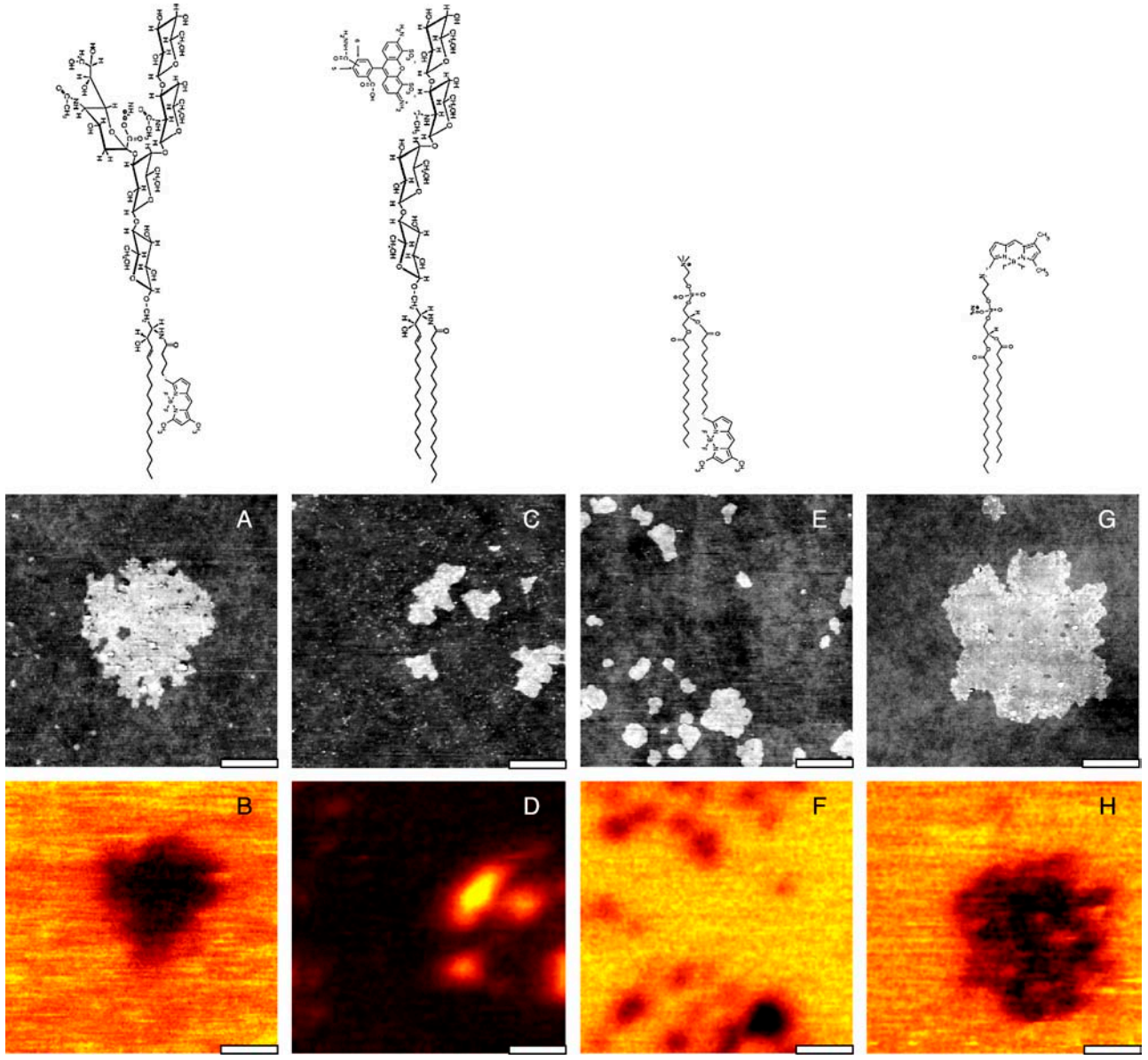

FIGURE 2 Simultaneous AFM topography (*middle row*) and fluorescence (*bottom row*) imaging of 3:1 DOPC/DPPC bilayers on glass with four different lipid probes. All images are 5 μm scans (scale bar = 1 μm). In the AFM images, the bright DPPC domains are 1.1 ± 0.2 nm higher than the surrounding DOPC. In the fluorescence images, the dark regions (less intensity) indicate exclusion of the probe lipids. In *A* and *B*, the probe is 0.05% BODIPY-C5-GM1. In *C* and *D*, the probe is 0.03% Alexa-488 head-GM1. In *E* and *F*, the probe is 0.05% BODIPY-C12-DHPC. In *G* and *H*, the probe is 0.05% BODIPY-DHPE. Structures of the probes (*top row*, above corresponding AFM and fluorescence images) are illustrative and meant for relative comparison. For the Alexa-488 head GM1, it is not known which sugar binds the Alexa-488 hydrazide.

tailgroups thus sufficiently perturbs the local packing of the lipid chains to be excluded from the ordered DPPC domains (19). This is expected for the short chain position of the BODIPY-C5-GM1. However, even the long-chain position of BODIPY-C12-DHPC does not improve its accommodation in the DPPC. Even more surprising, perhaps, is the exclusion of the BODIPY-DHPE, since the unaltered saturated acyl chains match DPPC. The exclusion from DPPC gel domains of other headgroup-labeled lipids derived from DPPE have also been reported for unsupported monolayers and bilayers (45,50). It should be pointed out, however, that partitioning is not solely driven by lipid phase. For example, in DLPC/DPPC mixtures with coexisting phases, *N*-rhodamine-DHPE was found to favor the DPPC gel phase (51). This is most likely due to more favorable hydrophobic matching.

The one exception to exclusion from DPPC seen in Fig. 2 is the preference for DPPC domains of Alexa-488 head-GM1 (Fig. 2, *C* and *D*). It is thus very significant that the large GM1 headgroup, even when conjugated with Alexa-488, is accommodated in the densely packed, ordered DPPC domains. Since all the partitioning results depicted in Fig. 2 have been observed in unsupported bilayers as well, we can conclude that probe partitioning in these supported bilayers does not appear to be qualitatively influenced by substrate interactions but rather by interactions in the bilayer.

The irregular shapes of the DPPC gel domains have also been observed in unsupported vesicles (20,49,52). The large domains in Fig. 2 are most likely formed by diffusion-limited Ostwald ripening at the expense of smaller domains during cooling of the sample to room temperature (53). However, apparent pockets of trapped DOPC and fluorescent probes in some DPPC domains (e.g., Fig. 2 *H*) suggest that aggregation also occurs to some extent during the cooling period. All features in the AFM images are static at room temperature. There are some very small (<50 nm) gel domains present as well. These small domains are well below the optical resolution in the fluorescence images and thus would never be seen in a fluorescence-only study. Finally, another observation reported in vesicle studies (20,49) is the symmetrical distribution of lipid domains across the bilayer, indicating strong coupling of the two monolayer leaflets. Evidence for similar behavior here can be found in the consistent correlation of domains in the topographic images with all features in the fluorescence images; e.g., there has been no observation in the fluorescence images of domains in the lower leaflet (proximal to the substrate) that do not have a corresponding topographic domain in the upper (distal) leaflet.

Site dependence of local mobility

In this section, we discuss the results of site-specific FCS measurements that relate to structural features in the AFM/fluorescence images, specifically DPPC domains and DOPC/DPPC domain boundaries. Since FCS can be readily performed at low probe concentrations (11), there is sufficient sensitivity for data acquisition in the dark regions of the fluorescence images. For the sake of clarity, we show only the fits to the FCS data in Figs. 4–7; representative FCS data can be seen in Figs. 8 and 9. With respect to domain boundaries, it is of particular interest to see if mobility in the DOPC phase is influenced by the proximity of ordered DPPC domains due to extended ordering (30) or to strains associated with boundary line tensions and/or gel domain formation (39). There are two important aspects of data acquisition that are imposed by the diffraction-limited optical resolution. These are illustrated in Fig. 3, where we have superimposed the DPPC domain boundaries, as determined from AFM, on the corresponding fluorescence image. Also depicted is the approximate FCS spot size (~400 nm) relative to the domain features. The first aspect to note is that the domain boundaries will always be blurred in the fluorescence images relative to the AFM topography. One can see in Fig. 3 that the true (AFM) boundaries are in the ''gray'' or intermediate intensity region of the fluorescence images. Since there can be an offset between the AFM and fluorescence images, we must use the fluorescence image to position the FCS spot. Thus we rely on these gray regions to select domain boundaries. Although the spot selection may be somewhat imprecise relative to the AFM image, the stability of the location is maintained by the closed-loop scanner. The second aspect to point out is that the smaller domains (<500 nm) tend to have diminished contrast in the fluorescence image. Since they stand out nicely in the AFM image, we can refer to the AFM data to verify that they are indeed domains.

In Fig. 4, we show very large differences in the mobility of Alexa-488 head-GM1 depending on the location of the

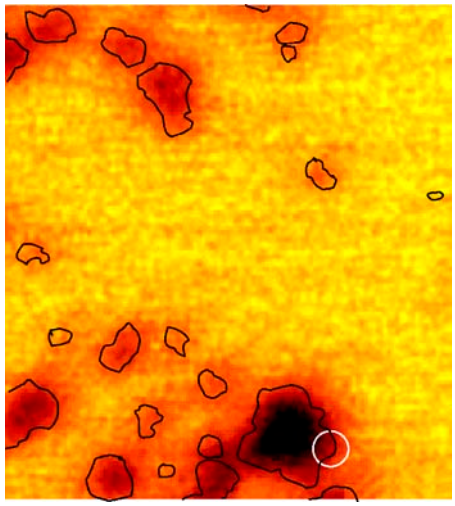

FIGURE 3 Overlap of simultaneous AFM and fluorescence images of 0.05% BODIPY-C12-DHPC taken from Fig. 2, *E* and *F*. For clarity, the AFM topographic image (Fig. 2 *E*) was processed in Adobe Photoshop (San Jose, CA) to display just the line edges of the DPPC domains. The white circle (used also as scale marker) is the approximate size of the calibrated FCS spot (400 nm diameter). It is located at a domain boundary that appears ''gray'' (intermediate intensity) in the fluorescence image.

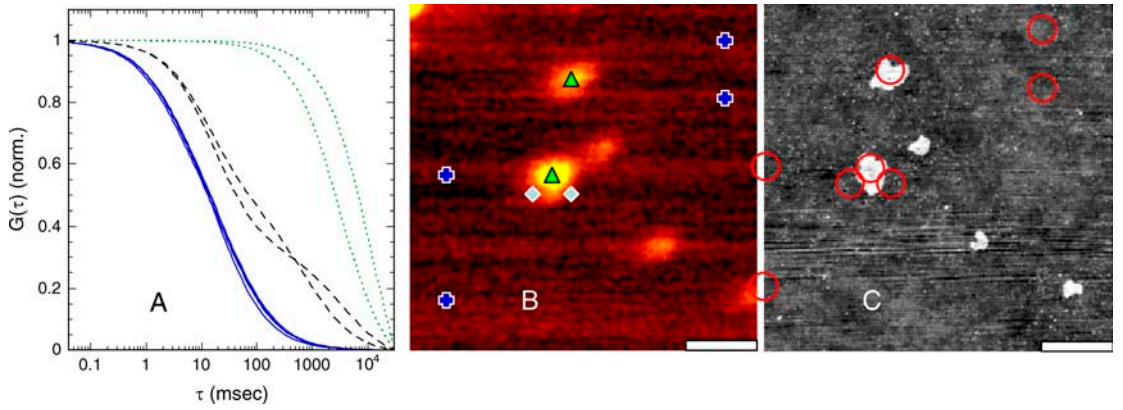

FIGURE 4 Representative FCS measurements in regions of supported bilayer of 3:1 DOPC/DPPC with 0.03% Alexa-488 head-GM1. (*A*) Fits to normalized autocorrelation curves (data curves not shown for clarity) acquired at specific sites indicated in fluorescence image (*B*). Diffusion coefficients are discussed in text. The solid curves are for DOPC regions marked by crosses, the dashed curves are for DOPC/DPPC boundary regions marked by diamonds, and the dotted curves are for DPPC domains marked by triangles. (*B*) Fluorescence image of Alexa-488 head-GM1, where bright regions are DPPC gel domains. (*C*) AFM topography acquired simultaneously with fluorescence image. Bright features are DPPC domains 1.1 ± 0.2 nm higher than the surrounding DOPC. The circles are the approximate size of the calibrated FCS spot and correspond to the locations selected in the fluorescence image. Images (*B* and *C*) are 5 μm scans (scale bar = 1 μm).

FCS measurement in the bilayer. The mobility in the DOPC region (*crosses* in Fig. 4 *B*, *solid curves* in Fig. 4 *A*) is consistently rapid ($D > 10^{-8}$ cm^2/s) and independent of location. Meanwhile, representative data for FCS locations inside the DPPC gel domains (*triangles* in Fig. 4 *B*, *dotted curves* in Fig. 4 *A*) reflect immobility ($D < 10^{-11}$ cm^2/s), which is verified by significant photobleaching. Similar FCS results were reported for DOPC/DPPC mixed vesicles (21). Thus the dense packing of the gel domains accommodates the Alexa-488 head-GM1, given the bright fluorescence in these regions, but also completely prevents mobility. For those points selected along the boundaries, the FCS data is characterized by distinct two-component fits reflecting the heterogeneity of the lipid packing at the domain boundary. Examples are shown in Fig. 4 (*diamonds* in Fig. 4 *B*, *dashed curves* in Fig. 4 *A*). The D_{fast} components of the two-component curve fits shown here range from 7–9 $\times$ 10^{-9} cm^2/s, the D_{slow} components range from 0.3–1.4 $\times$ 10^{-10} cm^2/s, and C_{fast}/C_{slow} ranges from 1–2. The multiple diffusion coefficients suggest a contribution from both fluid DOPC and gel DPPC phases, although according to the AFM map these FCS spots were predominately in the DOPC phase. We do not see evidence of a smooth transition in mobility between the two phases, and it is possible that the

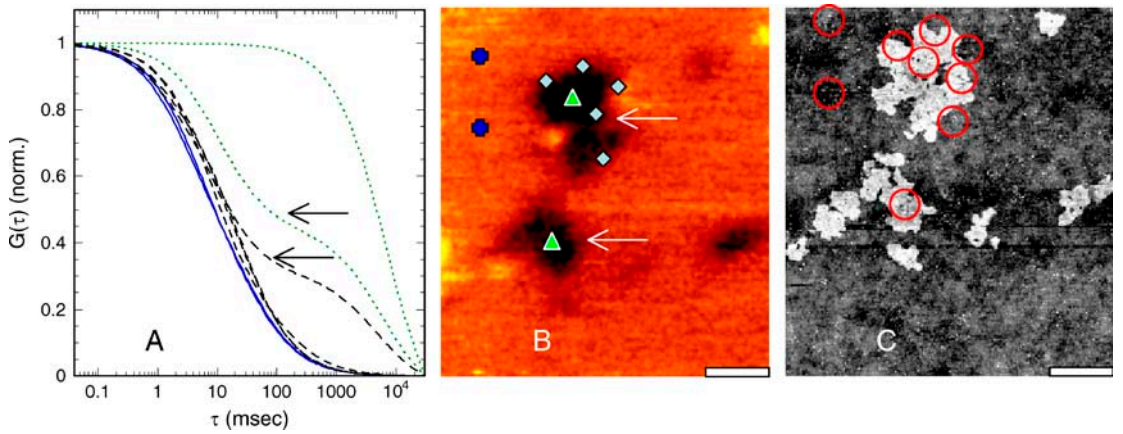

FIGURE 5 Representative FCS measurements in regions of supported bilayer of 3:1 DOPC/DPPC with 0.05% BODIPY-C5-GM1. (*A*) Fits to normalized autocorrelation curves (data curves not shown for clarity) acquired at specific sites indicated in fluorescence image (*B*). Diffusion coefficients are discussed in text. The solid curves are for DOPC regions marked by crosses, the dashed curves are for DOPC/DPPC boundary regions marked by diamonds, and the dotted curves are for DPPC domains marked by triangles. The selected dashed curve (*arrow*) corresponds to data acquired at diamond indicated by arrow in (*B*). The selected dotted curve (*arrow*) corresponds to data acquired at triangle indicated by arrow in (*B*). (*B*) Fluorescence image of BODIPY-C5-GM1, where dark regions represent exclusion from DPPC gel domains. (*C*) AFM topography acquired simultaneously with fluorescence image. Bright features are DPPC domains 1.1 ± 0.2 nm higher than the surrounding DOPC. The circles are the approximate size of the calibrated FCS spot and correspond to the locations selected in the fluorescence image. Images (*B*,*C*) are 5 μm scans (scale bar = 1 μm).

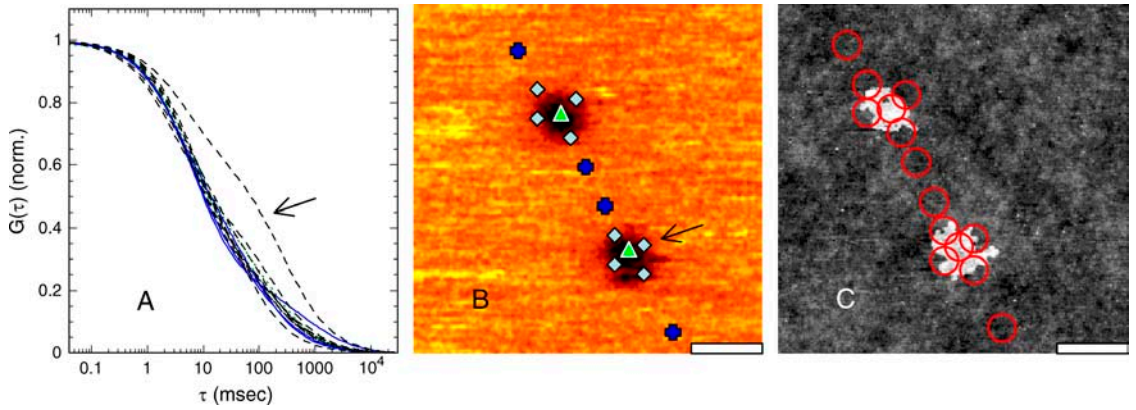

FIGURE 6 Representative FCS measurements in regions of supported bilayer of 3:1 DOPC/DPPC with ~0.05% BODIPY-DHPE. (*A*) Fits to normalized autocorrelation curves (data curves not shown for clarity) acquired at specific sites indicated in fluorescence image (*B*). Diffusion coefficients are discussed in text. The solid curves are for DOPC regions marked by crosses, the dashed curves are for DOPC/DPPC boundary regions marked by diamonds, and the dotted curves are for DPPC domains marked by triangles. The selected dashed curve (*arrow*) corresponds to data acquired at diamond indicated by arrow in *B*. (*B*) Fluorescence image of BODIPY-DHPE, where dark regions represent exclusion from DPPC gel domains. (*C*) AFM topography acquired simultaneously with fluorescence image. Bright features are DPPC domains 1.1 ± 0.2 nm higher than the surrounding DOPC. The circles are the approximate size of the calibrated FCS spot and correspond to the locations selected in the fluorescence image. Images (*A* and *B*) are 5 μm scans (scale bar = 1 μm).

nearby DPPC gel domain is influencing the Alexa-488 head-GM1 mobility in the DOPC phase.

In the case of BODIPY-C5-GM1, many probes along the domain boundaries appeared to be fully mobile. Representative data are shown in Fig. 5 where one can see that there is little difference in the mobility of those lipids along the domain boundary (*diamonds* in Fig. 5 *B*, *dashed curves* in Fig. 5 *A*) with those in the DOPC phase (*crosses* in Fig. 5 *B*, *solid curves* in Fig. 5 *A*). One exception (*diamond* indicated by *arrow* in Fig. 5 *B*) has a distinct two-component fit that most likely reflects a significant immobile fraction from the DPPC domain ($D_{fast} \approx 2 \times 10^{-8}$ cm^2/s, $D_{slow} \approx 3 \times 10^{-11}$ cm^2/s, and $C_{fast}/C_{slow} \approx 2$). Inside the larger DPPC domains (>1 μm), the BODIPY-C5-GM1 probes are immobile. However, we have detected instances (*highlighted triangle* in Fig. 5 *B*, *dotted curves* in Fig. 5 *A*) of significant mobility inside smaller domains. The corresponding autocorrelation curve is another distinct two-component fit, with $D_{fast} \approx 1 \times 10^{-8}$ cm^2/s, $D_{slow} \approx 2 \times 10^{-11}$ cm^2/s, and $C_{fast}/C_{slow} \approx 1.1$. Thus it appears that we have detected heterogeneities in DPPC gel domains.

We saw in Figs. 4 and 5 that the GM1 probes, particularly Alexa-488 head-GM1, exhibit the expected large changes in mobility when the FCS interrogation spot is moved from DOPC to DPPC domains. Alexa-488 head-GM1 probes are immobile in the smallest DPPC domains (<1 μm) that still fully contained the FCS spot without overlapping the boundary, whereas the BODIPY-C5-GM1 does exhibit limited mobility in some submicron DPPC domains. In stark contrast, however, we unexpectedly find that the

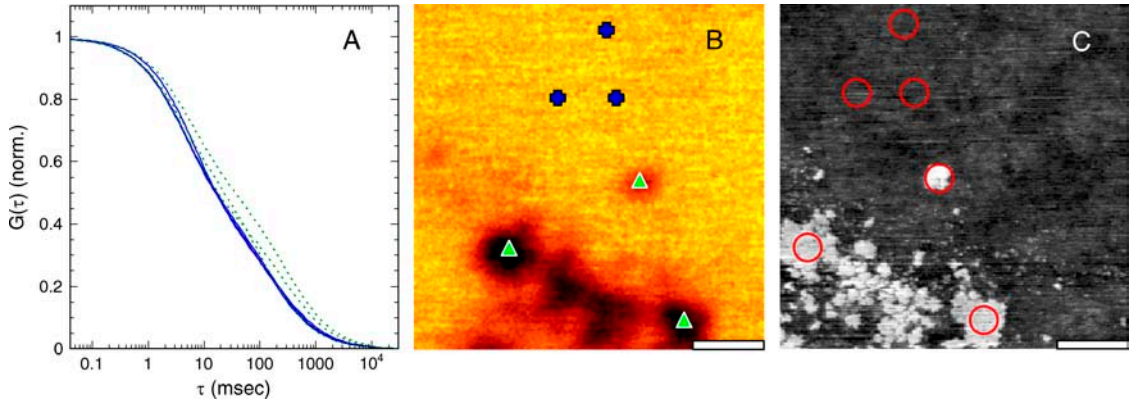

FIGURE 7 Representative FCS measurements in regions of supported bilayer of 3:1 DOPC/DPPC with ~0.05% BODIPY-C12-DHPC. (*A*) Fits to normalized autocorrelation curves (data curves not shown for clarity) acquired at specific sites indicated in fluorescence image (*B*). Diffusion coefficients are discussed in text. The solid curves are for DOPC regions marked by crosses, and the dotted curves are for DPPC domains marked by triangles. (*B*) Fluorescence image of BODIPY-C12-DHPC, where dark regions represent exclusion from DPPC gel domains. (*C*) AFM topography acquired simultaneously with fluorescence image. Bright features are DPPC domains 1.1 ± 0.2 nm higher than the surrounding DOPC. The circles are the approximate size of the calibrated FCS spot and correspond to the locations selected in the fluorescence image. Images (*A* and *B*) are 5 μm scans (scale bar = 1 μm).

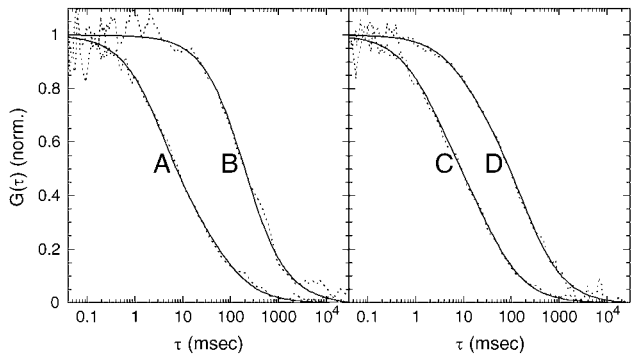

FIGURE 8 Effects of CTX-B binding on lateral diffusion of GM1 in DOPC regions of 3:1 DOPC/DPPC bilayers. Typical normalized autocorrelation curves of (*A*) 0.03% Alexa-488 head-GM1; (*B*) trace amounts of GM1 in DOPC bound to Alexa-488-CTX-B; (*C*) 0.05% BODIPY-C5-GM1; and (*D*) 0.05% BODIPY-C5-GM1 bound to B-CTX-B. The solid curves are fits to the data (*dotted curves*). Diffusion coefficients are discussed in text and summarized in Table 1.

mobility of the BODIPY-DHPE and BODIPY-C12-DHPC probes in DPPC domains of similar submicron size is almost indistinguishable from that in the fluid DOPC. An example of the surprising results is shown in Fig. 6, where a series of FCS curves were acquired for BODIPY-DHPE at indicated locations in and around DPPC domains that are ~0.5 μm in size. The mobility inside these DPPC domains (*triangles* in Fig. 6 *B*, *dotted curves* in Fig. 6 *A*) is almost the same as that

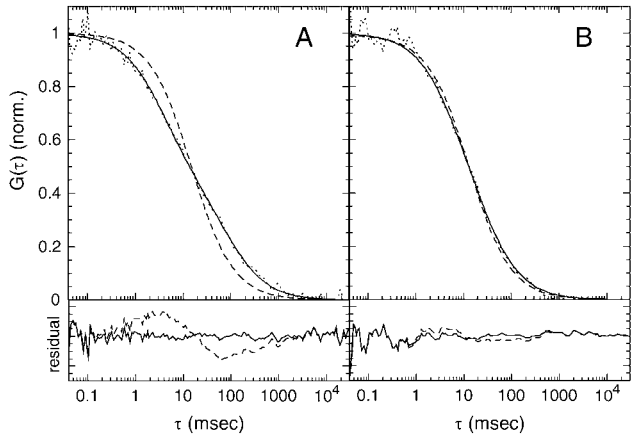

FIGURE 9 One-component versus two-component fits to normalized autocorrelation curves for lateral diffusion in DOPC. (*A*) Typical curve fits to BODIPY-DHPE and BODIPY-C12-DHPC autocorrelation curves (in this case, BODIPY-DHPE), where the dotted curve is the normalized autocorrelation data, the solid curve is the best two-component fit, and the dashed curve is the best one-component fit. It is clear from the curves and the residuals (*below*) that a two-component fit is required. (*B*) Typical curve fits to unbound Alexa-488 head-GM1 and BODIPY-C5-GM1 autocorrelation curves (in this case, Alexa-488 head-GM1), where the dotted curve is the normalized autocorrelation data, the solid curve is the best two-component fit, and the dashed curve is the best one-component fit. The residuals indicate a close fit for the one-component model, but the two-component model is slightly better. Diffusion coefficients are discussed in text and summarized in Table 1.

in the DOPC regions (*crosses* in Fig. 6 *B*, *solid curves* in Fig. 6 *A*). The only curve that has a significant slow component (indicated by *arrow*) was acquired on a domain boundary ($D_{fast} \approx 3 \times 10^{-8}$ cm^2/s, $D_{slow} \approx 4 \times 10^{-10}$ cm^2/s, $C_{fast}/C_{slow} \approx 0.7$). Similar behavior is observed for BODIPY-C12-DHPC in ~700 nm domains (Fig. 7). We found immobility only at the center of large DPPC domains (>1 μm) where the fluorescence intensity is at a minimum (not shown).

The apparent ''fluidity'' of these submicron DPPC domains for BODIPY-DHPE and BODIPY-C12-DHPC must indicate a large degree of heterogeneity. Marked heterogeneities have been reported for unsupported bilayers that contain phase-separated domains (50) as well as for pure DPPC in both supported and unsupported bilayers (32). In the case here, formation of the gel domains could be disrupted by DOPC clusters surrounding the BODIPY-labeled phospholipid probes like surfactants (54). In the darkest regions of the larger domains (>1 μm), the DPPC appears to be more homogeneous (at least the phospholipid probes are being excluded to a larger extent), which explains why the mobility there is curtailed. Future studies should examine domain heterogeneity versus probe concentration and domain size.

If the phospholipid probes somehow disrupt the DPPC packing, the opposite may be true for the unmodified GM1 and Alexa-488 head-GM1. Given the preference of GM1 and Alexa-488 head-GM1 for the DPPC gel domains, they most likely do not disrupt the dense, ordered packing of the DPPC. Thus those DPPC domains containing Alexa-488 head-GM1, for example, may be more homogenous, rendering the probe immobile. Possible evidence for this notion is the observation in Fig. 4 that the boundary FCS curves data showed an immobile component that indicates uniform, tight DPPC packing up the domain boundary. Another factor concerning immobility in the DPPC domains for both Alexa-488 head-GM1 and BODIPY-C5-GM1 probes is that they may undergo significant clustering (46,55); however, we see no evidence of large-scale clustering in the AFM topography or fluorescence. In the next section, we show that the only evidence for clustering occurs due to CTX-B binding, which reduces mobility in the fluid DOPC phase.

Diffusion in liquid-disordered DOPC regions: binding of CTX-B to GM1

In this section, we examine effects of CTX-B binding on the mobility of the GM1 components in the DOPC fluid phase. First of all, we find that the location of the fluorophore has little or no effect on the diffusion of the free (unbound) BODIPY-C5-GM1 and Alexa-488 head-GM1 in DOPC, whereas we saw above (e.g., Fig. 2) that it has a large effect on partitioning between fluid and gel domains. When BODIPY-C5-GM1 is bound to B-CTX-B, the diffusion is slowed by at least a factor of six relative to the unbound BODIPY-C5-GM1 (see Fig. 8, *C* and *D*). Since the asialoganglioside-derived Alexa-488 head-GM1 cannot bind CTX-B (56), we instead

compare its diffusion to trace amounts of native GM1 in DOPC that are bound to Alexa-488-CTX-B (Fig. 3, *A* and *B*). Once again, we observe that the diffusion of the Alexa-488-CTX-B-bound GM1 is slower, by a similar factor, than the unbound Alexa-488 head-GM1. These results are consistent with the notion that CTX-B forms pentamers that may bind up to five GM1 molecules in a cluster (47). A large cluster, that probably includes DOPC matrix lipids as well, is expected to move at a slower rate. Similar mobility changes with clustering have been observed for peptides in vesicles (57). The data contrast sharply, however, with measurements recently reported (14) for Alexa-488-CTX-B-bound GM1 diffusion in vesicles that are comparable to unbound lipid probes (5×10^{-8} cm^2/s).

Of particular interest is the mobility data for BODIPY-C5-GM1 after binding to B-CTX-B. Since the latter is bound only to the accessible BODIPY-C5-GM1 in the distal leaflet, one may expect the unbound BODIPY-C5-GM1 in the proximal leaflet to remain fully mobile, resulting in a distinct fast/slow two-component fit for the two leaflets. However, this is not what we observe. We find no evidence for a fully mobile fast component ($D_{fast} > 10^{-8}$ cm^2/s). Thus it appears that a strong coupling between the two leaflets (33) somehow slows the mobility of the unbound proximal BODIPY-C5-GM1. One possibility is that interleaflet coupling may induce clustering of the proximal BODIPY-C5-GM1 in a mirror image of the B-CTX-B-bound BODIPY-C5-GM1 in the distal leaflet. An important conclusion, therefore, is that interleaflet coupling in this model membrane appears to be more dominant than substrate effects (33).

Diffusion in liquid-disordered DOPC regions: two-component fits for PC probes

The lateral diffusion coefficients of the GM1 and PC lipid probes in the liquid-disordered DOPC phase are averages derived from many (>10) FCS sets taken in each region determined by AFM topography to be free of DPPC domains. All the bound and unbound GM1 probes (headgroup-labeled, tailgroup-labeled, and native) have FCS autocorrelation curves that generally fit fairly well with a one-component (D) lateral diffusion model. Two-component fits (D_{fast} and D_{slow}) are always better, of course, but also have greater variability among the FCS curves (hence the larger SDs). Thus we have tabulated both sets of fits in Table 1. Surprisingly, the data also suggest no clear evidence of a slow component that would arise from a strong interaction of the large GM1 headgroup with the substrate.

However, the case is very different for BODIPY-DHPE and BODIPY-C12-DHPC data in DOPC. These probes always require a two-component fit in the lateral diffusion analysis. The difference can be seen in Fig. 9, where we show a representative FCS curve from BODIPY-DHPE (Fig. 9 *A*) that requires a two-component fit and a representative FCS curve from Alexa-488 head-GM1 (Fig. 9 *B*) that has a one-component fit. There are possible systematic artifacts that may lead to poor one-component fits (58,59), due primarily to inadequate control over optical parameters. In the case here, we have appropriately optimized those parameters (see Materials and Methods) and have exercised great care to maintain a constant laser intensity, spot size, and spatial filter throughout this work. Although artifacts certainly cannot be dismissed, the fact that we are seeing two-component ''effects'' dominating for one set of probes and not another dispels systematic error as the cause. Thus we attribute the persistent two-component lateral diffusion of the phospholipid probes to a physical origin such as substrate interactions (33,36), bilayer heterogeneities (11,32,50), or multiple orientations of the probe itself relative to the membrane surface (60,61).

The D_{fast} diffusion components in Table 1 for unbound lipid probes (2–4 $\times$ 10^{-8} cm^2/s) are comparable to those previously measured for phospholipid and cyanine probes in both supported (22,23,33) and unsupported bilayers (11,21). It is tempting to attribute the D_{slow} diffusion component (0.08–0.4 $\times$ 10^{-8} cm^2/s) to probes in the proximal leaflet that are pinned by the substrate. Separate FRAP diffusion measurements of lipid probes in the proximal and distal leaflets on glass-supported bilayers revealed no difference in mobility ((1.3 ± 0.2) $\times$ 10^{-8} cm^2/s (33), (3.6 ± 0.5) $\times$ 10^{-8} cm^2/s (22)). Immobile fractions of 10–20% in both leaflets were also reported. In NMR studies of silica-bead-supported

TABLE 1 Two-dimensional translational diffusion coefficients for labeled lipid probes in DOPC and DPPC

	DOPC domains			
	D*	D_{fast}*	D_{slow}*	
Lipid probe	(one-component fit)	(two-component fit)		C_{fast}/C_{slow}
BODIPY-C5-GM1	1.4 ± 0.4	3.62 ± 0.77	0.29 ± 0.13	2.7 ± 1.1
BODIPY-C5-GM1 bound to B-CTX-B	0.13 ± 0.04	0.68 ± 0.15	0.035 ± 0.008	0.97 ± 0.4
Alexa-488 head-GM1	1.20 ± 0.29	3.61 ± 0.72	0.40 ± 0.09	1.78 ± 0.6
GM1, bound to Alexa-488 CTX-B	0.040 ± 0.011	0.50 ± 0.10	0.016 ± 0.007	0.54 ± 0.17
BODIPY-DHPE	N/A	3.71 ± 0.71	0.16 ± 0.05	1.6 ± 0.4
BODIPY-C12-DHPC	N/A	2.50 ± 0.78	0.076 ± 0.048	1.24 ± 0.3

DPPC domains D*
<0.001
<0.001†
<0.001
<0.001
>1.0‡
>1.0‡

*($\times 10^{-8}$cm^2/s), ± SD.
†Variable, some evidence observed for higher mobilities in submicron domains.
‡Submicron DPPC domains; immobility observed for domains >1 μm.

DPPC bilayers (36), the proximal leaflet was more ordered and had half the mobility (7.5×10^{-8} cm^2/s, at 55°C) of the distal leaflet.

There are several reasons, however, that we cannot solely attribute the slow diffusion component to the presence of the substrate. If the slow component is due to a significant fraction (C_{fast}/C_{slow} varies from ~1.2 to 3 in Table 1) of lipids that are influenced by substrate interactions, it is difficult to understand why the interactions are significantly less pronounced for the GM1 probes that have a much larger headgroup that the PC probes. This observation also discounts a notion that slow probe mobilities are due to a greater viscosity of the proximal leaflet induced by substrate interactions and/or an ordered water layer between the bilayer and the substrate. Furthermore, a strong interleaflet coupling, as noted in the previous section, would be expected to transfer significant substrate effects across the bilayer thereby reducing mobility for both leaflets. Finally, long-range electrostatic interactions with negative charges on the glass substrate are not considered to be a factor because we used a fairly high ionic strength buffer (150 mM NaCl PBS) that effectively shields substrate charges (62). When that buffer was replaced with 15 mM NaCl PBS buffer, and later with distilled water, no changes in the FCS data were observed. Interestingly, large decreases in mobility for both tailgroup-labeled BODIPY-C12-DHPC and headgroup-labeled rhodamine-DHPE have been observed in stacked lipid multilayers where Na^+ was increased from 0 mM (~7×10^{-8} cm^2/s) to 110 mM Na^+ (~1.4×10^{-8} cm^2/s (63)). The reduced mobility was attributed to clusters of three or more lipids bound together by the Na^+.

Bilayer heterogeneities in the fluid DOPC phase are difficult to assess. One advantage of this work is that AFM topographic maps provide sufficient detail with <10 nm resolution to rule out significant defects and domains not observable with other methods. Since obstructions to diffusion are mapped out and avoided, we do not attempt to fit the FCS curves with a time-dependent anomalous diffusion coefficient $D \propto t^{\alpha - 1}$, where α varies from 0.7 to 1.0 depending on the obstacle concentration (30,64). Obvious heterogeneities due to domain boundaries are shown in Figs. 4 and 5. Subtle heterogeneities, however, due to local packing or tilting would not be easily detected by AFM and may not be considered an obstruction in the anomalous diffusion model. In any case, for BODIPY-DHPE and BODIPY-C12-DHPC, the two-component curves are not subject to much variability since they are consistently observed for all spots in all the bilayers tested.

Fluorescent labels have been blamed for affecting the mobility of bound proteins, although it was thought to be due to the increased size of the complex (65). In the case here, significant effects to mobility (and partitioning) could be caused by the tendency for the BODIPY moiety to seek specific depths in the bilayer (60). In their study of unsupported DOPC model membranes containing BODIPY headgroup- and tailgroup-labeled PC probes, Kaiser and London (60) were able to show that a significant population of the BODIPY groups, despite their nonpolarity, exhibits a tendency to be located near the polar region of the bilayer. The remaining BODIPY groups are buried in the hydrophobic depths of the bilayer. Clearly, for the tailgroup-labeled BODIPY-C12-DHPC, the BODIPY has to ''loop back toward the surface'' (60), creating a large perturbation in the local packing of the surrounding lipids. Similarly, for BODIPY-DHPE, the BODIPY loops back toward the bilayer to seek polar groups and/or hydrophobic depths. The local distortion in the bilayer for such occurrences could involve many matrix DOPC lipids and thus could cause a loss of mobility due to the increased ''free area'' required for motion (64,66). Furthermore, given this scenario of BODIPY-induced molecular distortion, it would be very easy to understand why the phospholipid probes tend to be excluded from the tightly packed DPPC domains or cause significant perturbations in the DPPC packing. These effects are expected to be less pronounced for BODIPY-C5-GM1 because of the closer proximity of the BODIPY label on the short acyl chain to the polar region of the bilayer. Although the rhodamine-like label on Alexa-488 head-GM1 may not distort the orientation of the bulky headgroup, this may also explain why it is not excluded from the DPPC gel domains. Many important questions remain, however, as to how much of an effect local distortion in lipid structure has on mobility. The roughly linear dependence of lateral diffusion strictly on surface free area (66) is fairly mild relative to the difference between D_{fast} and D_{slow} diffusion components measured here.

SUMMARY AND CONCLUSIONS

We have demonstrated that two-dimensional diffusion in supported model membranes can be characterized locally by instrumentation that provides simultaneous AFM and fluorescence imaging of lipid domains. The AFM images not only provide nm-scale lateral resolution and topographic information but are used to reveal domain partitioning on the submicron scale of four different fluorescence probes that are used to obtain mobilities. The four probes were chosen because they are fluorescent analogs of naturally occurring lipids and they represent two common labeling schemes requiring headgroup and tailgroup modification. Overall, we find that the supported model membranes examined here have common attributes in structure and fluidity with unsupported vesicles; however, we have also presented unexpected results that suggest possible fluorophore effects on probe partitioning, domain heterogeneity, and probe mobility.

Partitioning of lipid components into membrane domains is central to the lipid raft model. We see here that the exclusion of labeled probes by their unlabeled counterparts in gel domains is indicative of significant perturbations in packing and/or lipid interactions, consistent with previous studies on supported and unsupported model membranes.

For both saturated phospholipid analogs BODIPY-C12-DHPC and BODIPY-DHPE, we see that modifications in either the acyl chain or the headgroup lead to exclusion from the saturated gel domains. For the GM1 analogs, we find that BODIPY-C5-GM1 is excluded from the gel domains, whereas Alexa-488 head-GM1 is not excluded. Thus the presence of the fluorescent label on the asialoganglioside headgroup does not interfere with the interactions that allow GM1 to occupy sites in the gel-phase DPPC.

Equally important in the lipid raft model of membrane function is the mobility of the lipid components inside and outside domains. Overall, we found that the mobilities of all four probes were roughly the same in the DOPC fluid phase. Thus we found no glaring difference in fluid phase mobility due to the location of the head- or tailgroup labeling. Both BODIPY-C5-GM1 and unmodified GM1 were shown to slow down by at least a factor of six upon binding to CTX-B fragments, which most likely indicates clustering induced by the pentameric CTX-B. Mobility of the unbound GM1 analogs is severely attenuated in the gel-phase DPPC. This is definitely the case for the Alexa-488 head-GM1, indicating a tight packing by the surrounding DPPC lipids. Furthermore, mobility appears to be restricted around the domain boundaries. The mobility in DPPC is also restricted for BODIPY-C5-GM1; however, evidence was presented for increased mobility in submicron domains that may be due to DPPC packing heterogeneities. Mobility around the domain boundaries is higher, resembling, for the most part, that in the fluid phase. This trend of increasing mobility in and around the submicron DPPC domains is remarkably prevalent in the BODIPY-C12-DHPC and BODIPY-DHPE phospholipid analogs. For these probes there appears to be little reduction in the lateral diffusion in the submicron DPPC domains relative to the DOPC regions. It is important to point out that these unexpected observations for the phospholipid analogs are not general for all DPPC domain sizes (immobility was detected in the center of large domains) and that a comprehensive study on mobilities versus domain size was not performed. However, the results presented here for submicron domains may be relevant to mobility in sphingolipid-cholesterol domains in biological membranes, where domain sizes are believed to be <100 nm (3,67). Thus its appears that those lipids such as Alexa-488 head-GM1 and unmodified GM1 that partition into the DPPC domains do not disrupt the dense packing and thus are rendered immobile, whereas those lipids that are excluded on the basis of disrupting the gel packing and/or lipid-lipid interactions may have greater mobility.

In general, we have shown that FCS can reveal heterogeneities in supported lipid bilayers. The phospholipid probes BODIPY-C12-DHPC and BODIPY-DHPE not only exhibited a perplexing mobility in submicron DPPC domains but also required two-component fits to the FCS curves in the fluid DOPC phase. The slow component could be due to a variety of factors including substrate interactions and membrane heterogeneities. However, it could also be due to local distortion of the molecule and surrounding matrix lipids by the tendency of BODIPY to seek polar regions of the membrane. This effect, documented elsewhere (60), may also be responsible for exclusion of the probes from close-packed gel domains. In any case, it is clear that the phospholipid probes, as well as other labeled phospholipids using different fluorophores, are not ideal for the modeling of partitioning and mobility in membranes. They do, however, illustrate that lipid components and lipid-protein complexes in biological membranes could move rapidly in and out of raft domains as needed.

The authors thank Mark Stevens for critical comments. Molecular structure images were kindly provided by Avanti Polar Lipids.

This research was supported in part by the Division of Materials Science and Engineering, Office of Basic Energy Sciences, U.S. Department of Energy, and National Institutes of Health K25AI060036. Sandia is a multiprogram laboratory operated by Sandia, a Lockheed Martin company, for the U.S. Department of Energy under contract DE-AC04-94AL85000.

REFERENCES

1. Brown, D. A., and E. London. 1998. Functions of lipid rafts in biological membranes. *Annu. Rev. Cell Dev. Biol.* 14:111–136.
2. Simons, K., and E. Ikonen. 1997. Functional rafts in cell membranes. *Nature.* 387:569–572.
3. Edidin, M. 2003. The state of lipid rafts: from model membranes to cells. *Annu. Rev. Biophys. Biomol. Struct.* 32:257–283.
4. Varma, R., and S. Mayor. 1998. GPI-anchored proteins are organized in submicron domains at the cell surface. *Nature.* 394:798–801.
5. Pyenta, P., D. Holowka, and B. Baird. 2001. Cross-correlation analysis of inner-leaflet-anchored green fluorescent protein co-redistributed with IgE receptors and outer leaflet lipid raft components. *Biophys. J.* 80: 2120–2132.
6. Gaus, K., E. Gratton, E. Kable, A. Jones, I. Gelissen, L. Kritharides, and W. Jessup. 2003. Visualizing lipid structure and raft domains in living cells with two-photon microscopy. *Proc. Natl. Acad. Sci. USA.* 100:15554–15559.
7. Tang, Q., and M. Edidin. 2003. Lowering the barriers to random walks on the cell surface. *Biophys. J.* 84:400–407.
8. Kenworthy, A., B. Nichols, C. Remmert, G. Hendrix, M. Kumar, J. Zimmerberg, and J. Lippincott-Schwartz. 2004. Dynamics of putative raft-associated proteins at the cell surface. *J. Cell Biol.* 165: 735–746.
9. Dietrich, C., B. Yang, T. Fujiwara, A. Kusumi, and K. Jacobson. 2002. Relationship of lipid rafts to transient confinement zones detected by single particle tracking. *Biophys. J.* 82:274–284.
10. Murase, K., T. Fujiwara, Y. Umemura, K. Suzuki, R. Iino, H. Yamashita, M. Saito, H. Murakoshi, K. Ritchie, and A. Kusumi. 2004. Ultrafine membrane compartments for molecular diffusion as revealed by single molecule techniques. *Biophys. J.* 86:4075–4093.
11. Schwille, P., J. Korlach, and W. W. Webb. 1999. Fluorescence correlation spectroscopy with single-molecule sensitivity on cell and model membranes. *Cytometry.* 36:176–182.
12. Schwille, P. 2001. Fluorescence correlation spectroscopy and its potential for intracellular applications. *Cell Biochem. Biophys.* 34: 383–408.
13. Rigler, R., and E. Elson. 2001. Fluorescence Correlation Spectroscopy: Theory and Applications. F. Schäefer, J. Toennies, and W. Zinth, editors. Springer-Verlag, Berlin/Heidelberg.

14. Bacia, K., I. Majoul, and P. Schwille. 2002. Probing the endocytic pathway in live cells using dual-color fluorescence cross-correlation analysis. *Biophys. J.* 83:1184–1193.

15. Bacia, K., D. Scherfeld, N. Kahya, and P. Schwille. 2004. Fluorescence correlation spectroscopy relates rafts in model and native membranes. *Biophys. J.* 87:1034–1043.

16. Dietrich, C., L. A. Bagatolli, Z. N. Volovyk, N. L. Thompson, M. Levi, K. Jacobson, and E. Gratton. 2001. Lipid rafts reconstituted in model membranes. *Biophys. J.* 80:1417–1428.

17. Dietrich, C., Z. N. Volovyk, M. Levi, N. L. Thompson, and K. Jacobson. 2001. Partitioning of Thy-1, GM1, and cross-linked phospholipid analogs into lipid rafts reconstituted in supported model membrane monolayers. *Proc. Natl. Acad. Sci. USA.* 98:10642–10647.

18. Wang, T.-Y., and J. R. Silvius. 2000. Different sphingolipids show differential partitioning into sphingolipid/cholesterol-rich domains in lipid bilayers. *Biophys. J.* 79:1478–1489.

19. Wang, T.-Y., and J. R. Silvius. 2003. Sphingolipid partitioning into ordered domains in cholesterol-free and cholesterol-containing lipid bilayers. *Biophys. J.* 84:367–378.

20. Korlach, J., P. Schwille, W. W. Webb, and G. W. Feigenson. 1999. Characterization of lipid bilayer phases by confocal microscopy and fluorescence correlation spectroscopy. *Proc. Natl. Acad. Sci. USA.* 96:8461–8466.

21. Scherfeld, D., N. Kahya, and P. Schwille. 2003. Lipid dynamics and domain formation in model membranes composed of ternary mixtures of unsaturated and saturated phosphatidylcholines and cholesterol. *Biophys. J.* 85:3758–3768.

22. Kalb, E., S. Frey, and L. Tamm. 1992. Formation of supported planar bilayers by fusion of vesicles to supported phospholipid monolayers. *Biochim. Biophys. Acta.* 1103:307–316.

23. Ratto, T., and M. Longo. 2003. Anomalous subdiffusion in heterogeneous lipid bilayers. *Langmuir.* 19:1788–1793.

24. Schütz, G., H. Schindler, and T. Schmidt. 1997. Single-molecule microscopy on model membranes reveals anomalous diffusion. *Biophys. J.* 73:1073–1080.

25. Martin, D., M. Forstner, and J. Käs. 2002. Apparent subdiffusion inherent to single particle tracking. *Biophys. J.* 83:2109–2117.

26. Dufrêne, Y., W. Barger, J.-B. Green, and G. Lee. 1997. Nanometer-scale surface properties of mixed phospholipid monolayers and bilayers. *Langmuir.* 13:4779–4784.

27. Yuan, C., J. Furlong, P. Burgos, and L. J. Johnston. 2002. The size of lipid rafts: an atomic force microscopy study of ganglioside GM1 domains in sphingomyelin/DOPC/cholesterol membranes. *Biophys. J.* 82:2526–2535.

28. Burns, A. 2003. Domain structure in model membrane bilayers investigated by simultaneous atomic force microscopy and fluorescence imaging. *Langmuir.* 19:8358–8363.

29. Boxer, S. G. 2000. Molecular transport and organization in supported lipid membranes. *Curr. Opin. Chem. Biol.* 4:704–709.

30. Ratto, T., and M. Longo. 2002. Obstructed diffusion in phase-separated supported lipid bilayers: a combined atomic force microscopy and fluorescence recovery after photobleaching approach. *Biophys. J.* 83: 3380–3392.

31. Benda, A., M. Benes, V. Marecek, A. Lhotsky, W. Hermens, and M. Hof. 2003. How to determine diffusion coefficients in planar phospholipid systems by confocal fluorescence correlation spectroscopy. *Langmuir.* 19:4120–4126.

32. Stevens, B., and T. Ha. 2004. Discrete and heterogeneous rotational dynamics of single membrane probe dyes in gel phase supported bilayer. *J. Chem. Phys.* 120:3030–3038.

33. Merkel, R., E. Sackmann, and E. Evans. 1989. Molecular friction and epistatic coupling between monolayers in supported monolayers. *Journal de Physique France.* 50:1535–1555.

34. Johnson, S. J., T. M. Bayerl, D. C. McDermott, G. W. Adam, A. R. Rennie, R. K. Thomas, and E. Sackmann. 1991. Structure of an adsorbed dimyristoylphosphatidylcholine bilayer measured with specular reflection of neutrons. *Biophys. J.* 59:289–294.

35. Sackmann, E. 1996. Supported membranes: scientific and practical applications. *Science.* 271:43–48.

36. Hetzer, M., S. Heinz, S. Grage, and T. Bayerl. 1998. Asymmetric molecular friction in supported phospholipid bilayers revealed by NMR measurements of lipid diffusion. *Langmuir.* 14:982–984.

37. Stottrup, B., S. Veatch, and S. Keller. 2004. Nonequilibrium behavior in supported lipid membranes containing cholesterol. *Biophys. J.* 86: 2942–2950.

38. Leonenko, Z., E. Finot, H. Ma, T. Dahms, and D. Cramb. 2004. Investigation of temperature-induced phase transitions in DOPC and DPPC phospholipid bilayers using temperature-controlled scanning force microscopy. *Biophys. J.* 86:3783–3793.

39. Xie, A., R. Yamada, A. Gewirth, and S. Granick. 2002. Materials science of the gel to fluid phase transition in a supported phospholipid bilayer. *Phys. Rev. Lett.* 89:246103.

40. O'Shannessy, D. 1990. Antibodies biotinylated via sugar moieties. *In* Avidin-Biotin Technology. M. Wilchek and A. Bayer, editors. Academic Press, London. 163.

41. Sheppard, C., and D. Shotton. 1997. Confocal Laser Scanning Microscopy. Springer-Verlag, New York.

42. Rigler, R., U. Mets, J. Widengren, and P. Kask. 1993. Fluorescence correlation spectroscopy with high count rate and low background: analysis of translational diffusion. *Eur. Biophys. J.* 22:169–175.

43. Hues, S., C. Draper, K. Lee, and R. Colton. 1994. Effect of PZT and PMN actuator hysteresis and creep on nanoindentation measurements using force microscopy. *Rev. Sci. Instrum.* 65:1561–1565.

44. Widengren, J., U. Mets, and R. Rigler. 1995. Fluorescence correlation spectroscopy of triplet states in solution: a theoretical and experimental study. *J. Phys. Chem.* 99:13368–13379.

45. Radhakrishnan, A., T. G. Anderson, and H. M. McConnell. 2000. Condensed complexes, rafts, and the chemical activity of cholesterol in membranes. *Proc. Natl. Acad. Sci. USA.* 97:12422–12427.

46. Yuan, C., and L. J. Johnston. 2001. Atomic force microscopy studies of ganglioside GM1 domains in phosphatidylcholine and phosphatidylcholine/cholesterol bilayers. *Biophys. J.* 81:1059–1069.

47. Miller, C., J. Majewski, R. Faller, S. Satija, and T. Kuhl. 2004. Cholera toxin assault on lipid monolayers containing ganglioside GM_1. *Biophys. J.* 86:3700–3708.

48. Burgos, P., C. Yuan, M. Viriot, and L. Johnston. 2003. Two-color near-field fluorescence microscopy studies of microdomains (''rafts'') in model membranes. *Langmuir.* 19:8002–8009.

49. Bagatolli, L. A., and E. Gratton. 2000. A correlation between lipid domain shape and binary phospholipid mixture composition in free standing bilayers: a two-photon fluorescence microscopy study. *Biophys. J.* 79:434–447.

50. Silvius, J. R. 2003. Fluorescence energy transfer reveals microdomain formation at physiological temperatures in lipid mixtures modeling the outer leaflet of the plasma membrane. *Biophys. J.* 85:1034–1045.

51. Bagatolli, L. A., and E. Gratton. 2000. Two photon fluorescence microscopy of coexisting lipid domains in giant unilamellar vesicles of binary phospholipid mixtures. *Biophys. J.* 78:290–305.

52. Veatch, S. L., and S. L. Keller. 2002. Organization in lipid membranes containing cholesterol. *Phys. Rev. Lett.* 89:268101.

53. Giocondi, M.-C., V. Vié, E. Lesniewska, P.-E. Milhiet, M. Zinke-Allmang, and C. Le Grimellec. 2001. Phase topology and growth of single domains in lipid bilayers. *Langmuir.* 17:1653–1659.

54. de Almeida, R., L. Loura, A. Fedorov, and M. Prieto. 2002. Nonequilibrium phenomena in the separation of a two-component lipid bilayer. *Biophys. J.* 82:823–834.

55. Milhiet, P.-E., V. Vié, M.-C. Giocondi, and C. Le Grimellec. 2001. AFM characterization of model rafts in supported bilayers. *Single Molecule.* 2:109–112.

56. MacKenzie, C., T. Hirama, K. Lee, E. Altman, and N. Young. 1997. Quantitative analysis of bacterial toxin affinity and specificity for glycolipid receptors by surface plasmon resonance. *J. Biol. Chem.* 272: 5533–5538.

57. Lee, C., and N. Petersen. 2003. The lateral diffusion coefficient of selectively aggregated peptides in giant unilamellar vesicles. *Biophys. J.* 84:1756–1764.

58. Hess, S., and W. Webb. 2002. Focal volume optics and experimental artifacts in confocal fluorescence correlation spectroscopy. *Biophys. J.* 83:2300–2317.

59. Enderlein, J., I. Gregor, D. Patra, and J. Fitter. 2004. Art and artifacts of fluorescence correlation spectroscopy. *Curr. Pharm. Biotechnol.* 5: 155–161.

60. Kaiser, R., and E. London. 1998. Determination of the depth of BODIPY probes in model membranes by parallax analysis of fluorescence quenching. *Biochim. Biophys. Acta.* 1375:13–22.

61. Klymchenko, A., G. Duportail, A. Demchenko, and Y. Mély. 2004. Bimodal distribution and fluorescence response of environment-sensitive probes in lipid bilayers. *Biophys. J.* 86:2929–2941.

62. Müller, D. J., D. Fotiadis, S. Scheuring, S. Müller, and A. Engel. 1999. Electrostatically balanced subnanometer imaging of biological specimens by atomic force microscope. *Biophys. J.* 76:1101–1111.

63. Böckmann, R., A. Hac, T. Heimburg, and H. Grubmüller. 2003. Effect of sodium chloride on a lipid bilayer. *Biophys. J.* 85:1647–1655.

64. Saxton, M. 1999. Lateral diffusion of lipids and proteins. *In* Current Topics in Membranes. D. Deamer, A. Kleinzeller, and D. Fambrough, editors. Academic Press, New York. 229–282.

65. Zhang, F., W. Schmidt, Y. Hou, A. Williams, and K. Jacobson. 1992. Spontaneous incorporation of the glycosyl-phophatidylinositol-linked protein Thy-1 into cell membranes. *Proc. Natl. Acad. Sci. USA.* 89: 5231–5235.

66. Liu, C., A. Paprica, and N. Peterson. 1997. Effects of size of macrocyclic polyamides on their rate of diffusion in model membranes. *Biophys. J.* 73:2580–2587.

67. Simons, K., and W. Vaz. 2004. Model membranes, lipid rafts, and cell membranes. *Annu. Rev. Biophys. Biomol. Struct.* 33:269–295.

(this page intentionally left blank)

Revealing the Topography of Cellular Membrane Domains by Combined Atomic Force Microscopy/Fluorescence Imaging

D. J. Frankel,* J. R. Pfeiffer,† Z. Surviladze,† A. E. Johnson,‡ J. M. Oliver,† B. S. Wilson,† and A. R. Burns*
*Biomolecular Materials and Interfaces Department, MS1413 Sandia National Laboratories, Albuquerque, New Mexico 87185;
†Department of Pathology and Cancer Research and Treatment Center, University of New Mexico, Albuquerque, New Mexico 87131;
and ‡School of Medicine, Texas A&M University, College Station, Texas 77843

ABSTRACT Simultaneous atomic force microscopy (AFM) and confocal fluorescence imaging were used to observe in aqueous buffer the three-dimensional landscape of the inner surface of membrane sheets stripped from fixed tumor mast cells. The AFM images reveal prominent, irregularly shaped raised domains that label with fluorescent markers for both resting and activated immunoglobin E receptors (FcεRI), as well as with cholera toxin-aggregated GM1 and clathrin. The latter suggests that coated pits bud from these regions. These features are interspersed with flatter regions of membrane and are frequently surrounded and interconnected by cytoskeletal assemblies. The raised domains shrink in height by ~50% when cholesterol is extracted with methyl-β-cyclodextrin. Based on composition, the raised domains seen by AFM correspond to the cholesterol-enriched dark patches observed in transmission electron microscopy (TEM). These patches were previously identified as sites of signaling and endocytosis based on their localization of activated FcεRI, at least 10 associated signaling molecules, and the presence of clathrin-coated pits. Overall the data suggest that signaling and endocytosis occur in mast cells from raised membrane regions that depend on cholesterol for their integrity and may be organized in specific relationship with the cortical cytoskeleton.

INTRODUCTION

Models of cell membrane organization are still evolving. Experimental evidence gathered over several decades suggests that the fluid mosaic model (1) fails to fully account for the possibility of ordered domains and other evidence of membrane heterogeneity (2–6). The modern concept that membranes are made up of distinct and dynamic mixtures of ordered and disordered lipid domains is based in part on model membrane studies that dramatically demonstrate phase separation of lipids, due largely to their state of saturation (7,8). Evidence for the partitioning of cholesterol and specific cellular lipids and proteins into ''lipid rafts'' in cells comes principally from their detergent insolubility and subsequent recovery in light fractions of sucrose density gradients (9,10).

Recent evidence from electron microscopy that typical ''raft markers'', such as glycosylphosphatidylinositol (GPI)-anchored proteins and GM1 ganglioside, fail to colocalize either with each other or with signaling receptors confirms the nonrandom topographical organization of native cell membranes and suggests that microdomains may be much more numerous and heterogeneous than suggested from biochemical studies (2,11). Membrane domains may also be much smaller than originally suggested. Several groups have proposed that domains in resting cells are $<$70 nm in size (12,13). Using laser trapping and single particle tracking (SPT) techniques, Pralle et al. (14) estimated GPI-linked proteins to reside in rafts as small as 26 $\pm$ 13 nm in diameter. In transmission electron microscopy (TEM) studies of membrane sheets, Prior et al. (15) found Ras in microdomains of mean radius 22 $\pm$ 4 nm. Remarkably, these domains occupied 35% of the plasma membrane.

Immunogold labeling and electron microscopic imaging of endogenous proteins in the cytoplasmic face of mast cell membranes, including the abundant immunoglobin E (IgE) receptor (FcεRI) and its signaling partners, has revealed that most (if not all) proteins in native membranes are distributed as small, dispersed clusters before stimulus (2,16,17). Despite this order, the membrane is adaptable and capable of dynamic reorganization. This is well illustrated by TEM observations showing that FcεRI can coalesce within minutes of activation into patches as large as 200–400 nm in diameter (2,16,17). Because these sites of receptor aggregation accumulate many signaling proteins, they are presumed to be sites of active signaling. The signaling patches typically occupy ''dark'' membrane regions that show enhanced labeling with osmium, indicating high levels of double bond-containing lipids and/or cholesterol (2), and are frequently bordered by coated pits (see Fig. 1 *B*). It is of great interest, therefore, to determine if the signaling patches are indeed distinct topographic features in mast cell membranes.

Here, we complement electron microscopy with atomic force microscopy (AFM) to further examine the topography of the cytoplasmic face of plasma membrane sheets stripped from tumor mast cells (rat basophilic leukemia RBL-2H3). AFM has been used extensively to characterize biological samples because it can be routinely performed in natural fluid environments, which is a clear advantage over vacuum conditions imposed by the TEM. It has also been well established that AFM can provide undistorted images of soft, compliant membrane structures, due in large part to sensitive

Submitted August 31, 2005, and accepted for publication December 14, 2005.
Address reprint requests to A. R. Burns, E-mail: aburns@sandia.gov.

0006-3495/06/04/2404/10 $2.00
doi: 10.1529/biophysj.105.073692

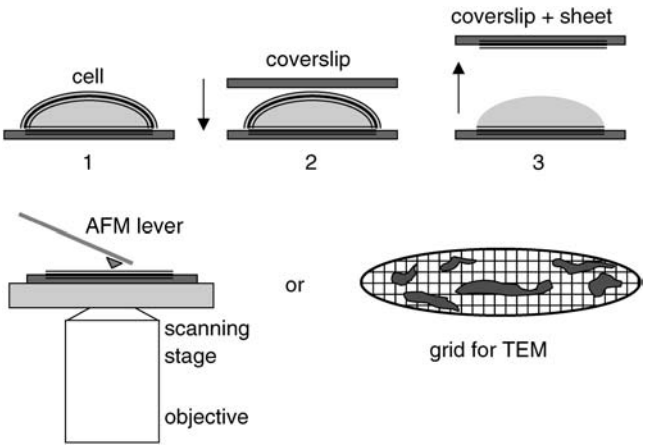

FIGURE 1 Schematic view of the membrane sheet preparation for AFM analysis. Whole cells are dispensed onto substrates (step *1*). A poly-L-lysine-coated coverslip is lowered (step *2*) onto the dorsal surface of lightly fixed cells to make a ''sandwich'' that can be separated (step *3*), producing a monolayer of membrane sheets, all oriented with the cytoplasmic face-up for simultaneous AFM/fluorescence imaging (*lower left*). A very similar procedure generates cytoplasmic face-up membrane sheets on nickel grids for TEM imaging (*lower right*).

force feedback detection and use of the tapping mode to reduce lateral forces (18–21). In model membrane studies, AFM has been able to map phase-separated lipid domains (22–24). A key feature of this study is the ability to correlate membrane topographic features with the locations of fluorescently tagged proteins and lipids through simultaneous acquisition of AFM and confocal fluorescence images (23,24).

Our AFM results show that the inner side of the plasma membrane is composed of numerous irregular-shaped raised domains that contain both resting and activated FcεRI, aggregated GM1, and clathrin. When present, a fibrous meshwork appears to link adjacent raised domains, suggesting a role for the cortical cytoskeleton in organizing these prominent features of the plasma membrane landscape. Taken together, the results identify the raised domains seen in AFM as the darkened membrane regions seen by TEM. Although the raised domains are likely to be heterogeneous in content, they importantly include sites of signaling and endocytosis.

MATERIALS AND METHODS

Antibodies and reagents

The dinitrophenol (DNP)-specific IgE was affinity purified from the ascitic fluid of mice bearing the H1 DNP-ε-26.82 hybridoma (25) and conjugated to Alexa 488 using a kit supplied by Molecular Probes (Eugene, OR). Monoclonal antibodies to anti-clathrin heavy chain were purchased from Calbiochem (San Diego, CA). Alexa-488-conjugated anti-mouse IgG $F(ab')_2$ and Alexa-488-conjugated recombinant cholera toxin B fragment (Alexa-488-CTX-B) were purchased from Molecular Probes. Monomeric perfringolysin O (PFO) was produced as His-tagged recombinant protein in *Escherichia coli* and purified by Ni-NTA affinity chromatography.

Cell culture and treatment

Stock cultures of RBL-2H3 mast cells were maintained in minimal essential medium (Gibco, Invitrogen, Carlsbad, CA) supplemented with 10% Hybrimax (Sigma, St. Louis, MO) and passaged twice weekly. Cells were dispensed into suspension dishes containing 15 mm diameter clean glass coverslips. In some cases, the cells were preincubated for 1 h with Alexa 488 IgE (2 μg/ml) to prime and label the FcεRI. Cells were then incubated for 7 min at 37°C, plus or minus polyvalent antigen (DNP-bovine serum albumin (BSA), 0.1 μg/ml), followed by fixation and sheet preparation (described below). For the GM1 study, cells were treated with Alexa 488 cholera toxin for 10 min at either room temperature (RT) or 37°C before fixation. For cholesterol depletion, cells were pretreated for 30 min with 10 μM methyl-β-cyclodextrin (MβCD) (Sigma) in MEM containing 10% fatty-acid-free BSA before fixation and sheet preparation.

Preparation of plasma membrane sheets for AFM/fluorescence

As shown schematically in Fig. 1, the cytoplasmic face of membrane sheets were prepared for simultaneous AFM/fluorescence imaging by modification of the procedure used for TEM imaging (16), described below, and originated by Sanan and Anderson (26). Ethanol-cleaned 25 mm diameter glass coverslips were glow discharged, coated with 0.2 mg/ml of poly-L-lysine for 30 min, rinsed in doubly distilled water for 10 s, and air dried. Cells were fixed in 0.5% paraformaldehyde in phosphate-buffered saline (PBS) in the presence of Hoechst 33942 nuclear stain for 7 min at RT, rinsed, and held in PBS. Next, the monolayer was dipped in HEPES buffer and inverted onto the center of a poly-L-lysine-coated coverslip, without applying pressure. The resulting ''sandwich'' was left for 10 min at RT on moist 4.25 cm filter paper then separated by floating apart in HEPES buffer. For the clathrin labeling experiment, coverslips carrying membrane sheets were incubated in mouse monoclonal anti-clathrin heavy chain for 30 min. This was followed by rinsing three times in PBS and incubation in the secondary antibody Alexa 488 $F(ab')_2$ goat anti-mouse IgG with a 0.1% solution of BSA for 30 min at room temperature. Coverslips were rinsed three times in PBS, mounted in a coverslip dish (Harvard Apparatus, Holliston, MA), and immediately immersed in PBS for imaging.

Plasma membrane sheet preparation and gold labeling for TEM

Plasma membrane sheets were prepared and processed for TEM as described in Wilson et al. (16) and shown schematically in Fig. 1. Briefly, coverslips of live or lightly fixed (0.5% paraformaldehyde for 10 min at 37°C) cells were immersed in ice-cold HEPES buffer (25 mM HEPES, pH 7, 25 mM KCl, 2.5 mM $Mg(C_2H_3O_3)_2$) and inverted onto nickel electron microscopy (EM) grids that had been coated with formvar and carbon and, on the day of the experiment, glow discharged and floated on poly-L-lysine (0.8 mg/ml for 30 min, followed by 10 s doubly distilled water rinse and air drying). Pressure was applied to the coverslip for 20 s by bearing down with a cork. The coverslips were lifted, leaving sections of the upper cell surface adherent to the poly-L-lysine-coated grid. Membranes were immediately fixed in 2% paraformaldehyde for 10 min at 4°C. FcεRI β-subunits were labeled from the inside sequentially with primary antibodies and gold-conjugated secondary reagents by inverting grids onto droplets. Cholesterol on the inner face of the plasma membrane was labeled using 5 nm colloidal gold (BBInternational, Cardiff, UK) conjugated to recombinant, monomeric PFO, using the manufacturer's instructions. Samples were postfixed in 2% glutaraldehyde in PBS, stained for 10 min with 1% OsO_4 prepared in 0.1 M cacodylate buffer, and washed 5 min with cacodylate buffer followed by doubly distilled water. Samples were finally processed for 10 min each in 1% aqueous tannic acid and 1% aqueous uranyl acetate, with intermediate and final washes in doubly distilled water. Grids were air dried and examined using a Hitachi 600 transmission electron microscope.

Simultaneous AFM and fluorescence imaging

The apparatus to obtain simultaneous AFM and confocal fluorescence imaging has been described in detail elsewhere (23,24). Briefly, an inverted microscope (Olympus IX70, Tokyo, Japan) was modified to accommodate a Bioscope AFM head (Veeco, Santa Barbara, CA). The coverslip dish containing membrane sheets was mounted onto an X-Y piezo scanner plate (Nanonics, Tel Aviv, Israel). The scanner plate in turn was mounted on a manual X-Y stage that allowed large range viewing of the sample with a Hg lamp. In this way, whole cells indicated by the Hoechst nuclear stain were detected and avoided. The AFM probe was centered on the membrane sheets, and the Hg lamp was extinguished. Excitation light from a 488 nm Ar^+ laser was focused by a 100×, numerical aperture 1.2 oil objective (Olympus) to a 300 nm spot and aligned with the AFM probe by visual inspection. (A slight nanometer-scale offset between fluorescence and AFM images can occur due to the alignment.) Epifluorescence was spatially filtered in a confocal manner by coupling into a 50 μm diameter core multimode fiber connected to an avalanche photodiode detector. AFM and fluorescence images were acquired with a single controller (RHK, with SPM32 software). All the AFM data presented here were acquired under forces <1 nN, with levers (Olympus TR400-PSA, nominal force constant of 0.08 N/M) in tapping mode. The XY scanner plate was calibrated with a 463 nm square grid grating (Ted Pella, Redding, CA), and the AFM head was calibrated in Z with known 25.5 nm steps (TGZ01, NT-MDT Mikromasch, Allen, TX). Three-dimensional (3-D) rendering was accomplished using WSXM freeware (Nanotec, Madrid, Spain).

Analysis of AFM topography

Specific features in the AFM topography were analyzed by line profiling routines provided in WSXM and SPM32 imaging software (see Fig. 7 for examples). Each line profile gave both height and width information. The heights of raised domains are measured relative to the surrounding membrane (not relative to the substrate). Since raised domains were irregularly shaped, care was taken for each domain to acquire representative profiles. All the representative height and width data were entered into KaleidaGraph software (Synergy Software, Reading, PA) for statistical analysis (Table 1) and histogram binning (see Fig. 9).

RESULTS AND DISCUSSION

Aggregated receptors are found in raised domains

As shown previously (2,16,17), TEM imaging of immunogold-labeled IgE receptors, FcεRI, in RBL membrane sheets reveals recruitment to electron-dense dark patches upon activation. The dark patches preexist in resting cells but become more prominent with FcεRI clustering. In Fig. 2 *A*, IgE-primed receptors are distributed across the resting membrane in small clusters. Clathrin lattices (*arrow*) and clathrin-coated pits are features of the resting membrane. Upon activation by the addition of multivalent antigen (Fig. 2 *B*), FcεRI form large clusters that localize to the characteristic dark patches. Clathrin lattices and clathrin-coated pits are seen inside and in close proximity to the dark patches. Budding pits often contain the IgE receptors after activation, indicating that dark contrast regions are involved in both signaling and endocytosis (2). Prior work also showed that GM1 is recruited independently to the same dark patches containing activated FcεRI, after its CTX-B aggregation (2). Thus activated FcεRI, aggregated GM1, and clathrin colocalize in the dark patches.

TABLE 1 Topographic information

Structure (No. of measurements)	Domain height (nm)	Domain width (nm)
	±Standard deviation	±Standard deviation
Flat region of membrane* (5)	7.0 ± 0.2	–
Flat region of membrane* (5) Treated with MβCD	6.8 ± 0.7	–
Raised domain, activated (68)	50 ± 16	575 ± 315
Raised domain, resting (38)	43 ± 13	394 ± 191
Raised domain, activated (34) Treated with MβCD	36 ± 17	650 ± 354
Raised domain, resting (46) Treated with MβCD	24 ± 9	358 ± 244

*Relative to poly-L-lysine covered substrate.

We began our simultaneous AFM/confocal fluorescence imaging of resting and activated RBL-2H3 mast cell sheets with the objective of observing any topographically distinct membrane features that contained fluorescence-tagged FcεRI IgE receptor. Our technique of membrane harvesting, shown schematically in Fig. 1, exposes only the cytoplasmic surface to AFM imaging. However, either surface can be labeled with a fluorescent tag. Thus in the first experiments, the cells were primed with Alexa-488-conjugated anti-DNP IgE to occupy the high affinity IgE receptors that are present on the extracellular surface at levels approaching 200,000/cell. This priming step provides a fluorescence tag for receptor tracking but does not induce signaling responses.

The results for resting and activated cells are shown in Fig. 3, *A–F*. AFM topographic images of the cytoplasmic surface of resting membrane sheets reveal raised domains (Fig. 3 *A*, *arrows*). The edge of the membrane sheet can also be seen. In the resting sheets, the simultaneous fluorescence image (Fig. 3 *B*) exhibits semiuniform fluorescence; however, occasional large clusters can be resolved (*white arrows*, Fig. 3 *B*). These data are consistent with dispersed clusters of resting FcεRI, containing only a few receptors, that are below the resolution of the confocal microscope (~300 nm). We do see, however, that bright regions (*white arrows*) within the uniform fluorescence map to the raised domains in the AFM topography (Fig. 3 *A*). To accentuate the correlation, we have used edge-finding routines in Adobe Photoshop (Adobe Systems, San Jose, CA) to overlay the domain boundaries on the fluorescence image (Fig. 3 *C*). After activation induced by cross-linking IgE-bound receptors with the polyvalent ligand DNP-BSA, we clearly see raised domains in the AFM topography of the membrane sheets (Fig. 3 *D*). Moreover, the semiuniform fluorescence observed in the resting sheets gives way to strongly clustered, bright foci of FcεRI in the activated sheets (Fig. 3 *E*). The strong clustering correlates precisely with the raised domains in the topography (Fig. 3 *F*).

Cross-linked gangliosides redistribute to raised domains

Since prior TEM work showed that GM1 aggregated by CTX-B fragments is recruited independently to the same

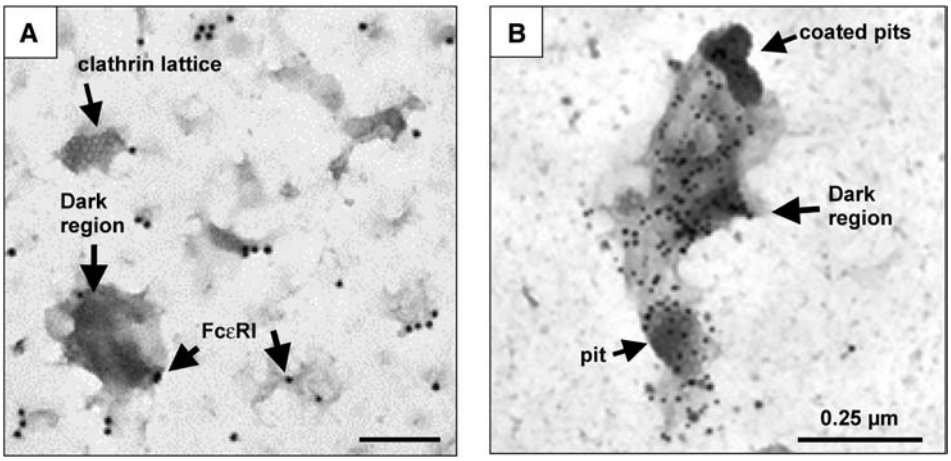

FIGURE 2 TEM images of FcεRI IgE receptor distributions in membrane sheets, as revealed by 10 nm anti-FcεRI β-gold labels. The membranes were prepared from IgE-primed cells, without (*A*) or with (*B*) 5 min of antigen (DNP-BSA) activation. Immunogold labeling is performed after membrane harvesting. In resting membranes (*A*), the receptor is distributed uniformly in small clusters. In activated cells (*B*), it forms large clusters localized in dark regions. Clathrin-coated pits are visible and tend to occur on the edges of the dark regions.

dark patches containing cross-linked FcεRI (2), we checked to see if cross-linked GM1 is present in the raised domains. In this case, we incubated live, resting RBL-2H3 cells with Alexa-488-conjugated CTX-B before sheet preparation. As shown in Fig. 4, *A* and *B*, raised domains in the AFM topographic image (Fig. 4 *A*) in the resting membrane sheets do indeed correlate with bright clusters of GM1 stained with labeled CTX-B (Fig. 4 *B*). This correlation is made clear in

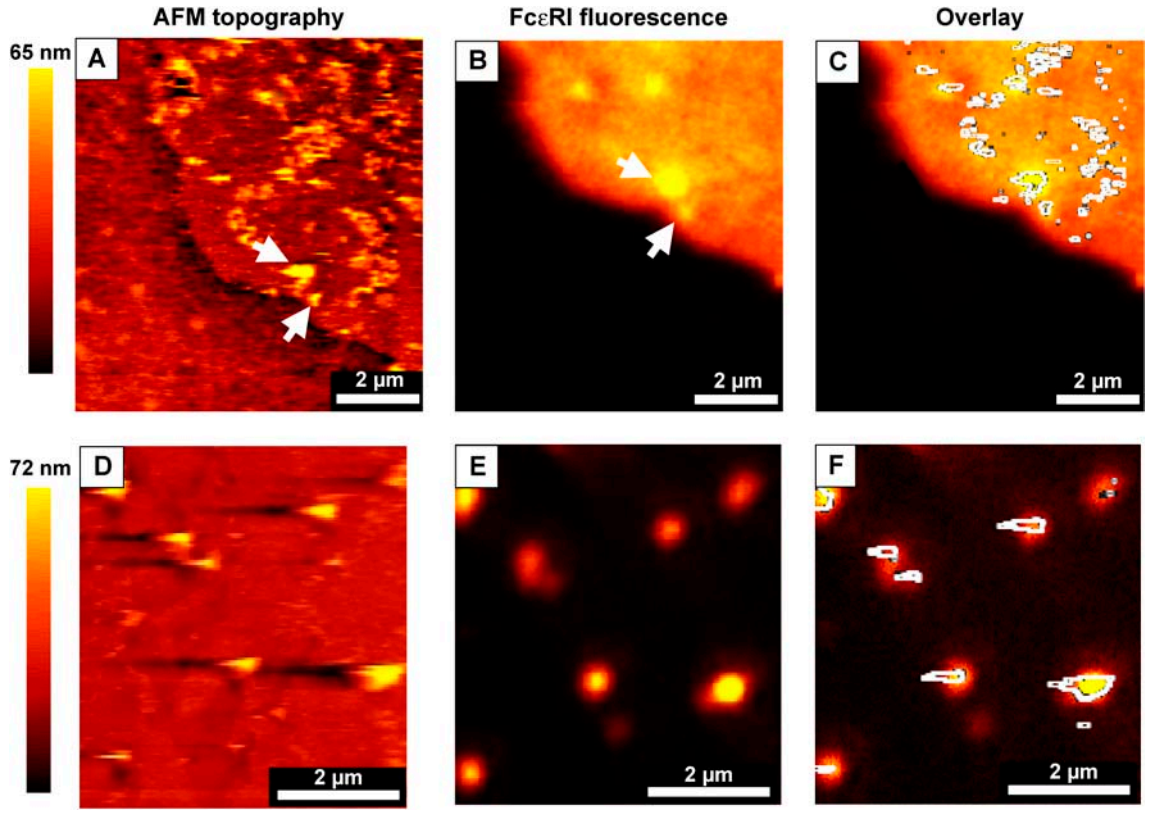

FIGURE 3 Simultaneous AFM and confocal fluorescence images of FcεRI IgE receptor distributions in membrane sheets. The membranes were prepared from Alexa-488-labeled IgE-primed cells, without (*A–C*) or with (*D–F*) 5 min of antigen (DNP-BSA) activation. In the resting membrane (*A–C*), the white arrows point to examples of correlation between bright fluorescent IgE spots (*B*) marking small clusters of resting receptors near the edge of the membrane sheet that correlate with raised domains in the AFM image (*A*). In *C*, we have overlaid the topographic domain edges from *A* onto the fluorescence image (*B*) to confirm that the tagged IgE receptors cluster in ''raised'' membrane regions. The clustering is much more pronounced for activated receptors (images *D* and *E*), where the bright regions in the IgE fluorescence (*E*) map clearly with the raised domains in the AFM image (*D*). In *F*, we have overlaid the topographic domain edges from *D* onto the fluorescence image (*E*) to confirm the coincidence of receptors and raised domains. The pseudocolor scales indicate the relative height of membrane features in the AFM images (*A* and *D*).

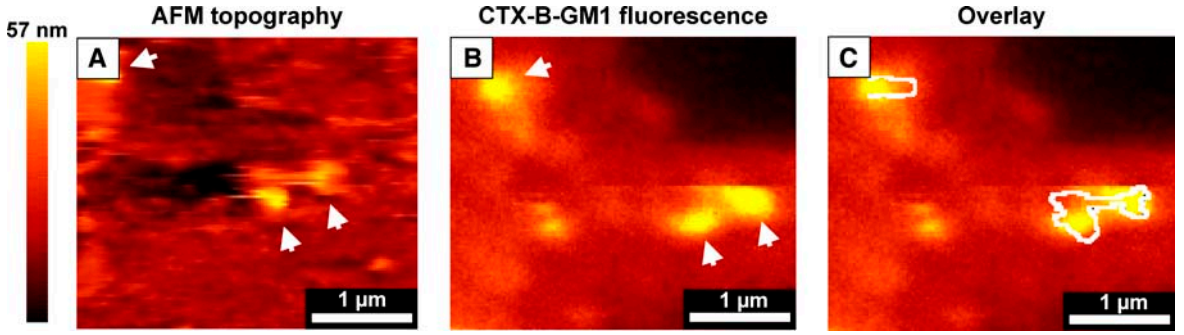

FIGURE 4 Simultaneous AFM (*A*) and confocal fluorescence (*B*) images of resting RBL cell membrane sheets where the GM1 ganglioside is aggregated by Alexa-488-labeled CTX-B before fixation. In *B*, the upper right corner is dark due to photobleaching. Arrows in the paired images point to examples of correlation between fluorescent label in *B* and raised domains in *A*. In *C*, we have overlaid the topographic domain edges from *A* onto the fluorescence image (*B*) to confirm the colocalization. The pseudocolor scale indicates the relative height of membrane features in the AFM image (*A*).

the overlay (Fig. 4 *C*). In contrast, there was no correlation between fluorescence and AFM topographic features when Alexa-488-cholera toxin was applied to prefixed cells (not shown). The latter is consistent with the essentially random distribution of GM1 observed in TEM for prefixed cells (2) and supports the concept that there are distinct membrane features on the cytoplasmic face associated with the RBL signaling patches.

Clathrin-coated vesicles bud from raised domains

Previous TEM studies (2,16) have shown that clathrin-coated vesicles tend to bud from the dark patches in membrane associated with FcεRI signaling (see pits marked with *arrows* in Fig. 2 *B*). To access the relationship of clathrin to the raised domains on the cytoplasmic surface that are observed with AFM, membrane sheets were treated with monoclonal antibodies to clathrin heavy chain, followed by labeling with fluorescent anti-mouse antibodies. The results are shown in Fig. 5. Once again, there is a very good correlation between raised domains (Fig. 5 *A*) and the distribution of clathrin (Fig. 5 *B*). Thus it is clear that the raised domains contain clathrin-coated pits. Occasionally, it is possible to resolve domed structures within large, irregularly shaped raised domains. This can be seen in Fig. 6, *A* and *B*, where Fig. 6 *B* is an expanded 3-D view of such a feature present in Fig. 6 *A*. One possible interpretation of the peaks in the 3-D view is that clathrin-coated vesicles are budding from a larger raised domain.

To summarize our results so far, we have seen raised domains in all the AFM topographic images of the membrane sheets (both resting and activated). All the raised domains appear to label with IgE receptor, GM1 that has been aggregated by CTX-B, and clathrin. Since all three are known from the TEM results (2,16,17) to colocalize in the dark patches, particularly for the activated cells, it is straightforward to conclude that the dark patches correspond to the raised domains in AFM topography and represent distinct topographic feature of these membranes.

Repeated measurements discussed in detail below, and summarized in Table 1 and Fig. 9, reveal that the height of the raised domains, relative to the surrounding membrane,

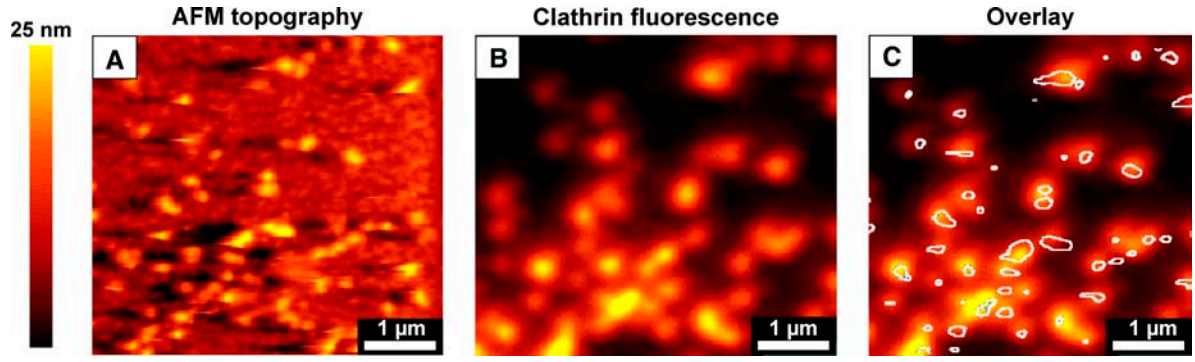

FIGURE 5 Simultaneous AFM (*A*) and confocal fluorescence (*B*) images of resting RBL cell membrane sheets where clathrin is labeled with mouse monoclonal anti-clathrin heavy chain and Alexa 488 $F(ab')_2$ goat anti-mouse IgG. The raised domains in *A* correlate strongly with the bright regions in *B*, thus clearly indicating the presence of clathrin. In *C*, we have overlaid the topographic domain edges from *A* onto the fluorescence image (*B*) to confirm the colocalization. The pseudocolor scale indicates the relative height of membrane features in the AFM image (*A*). In this particular sheet, the raised domains are reduced in height by treatment with 10 μM MβCD (see Fig. 7).

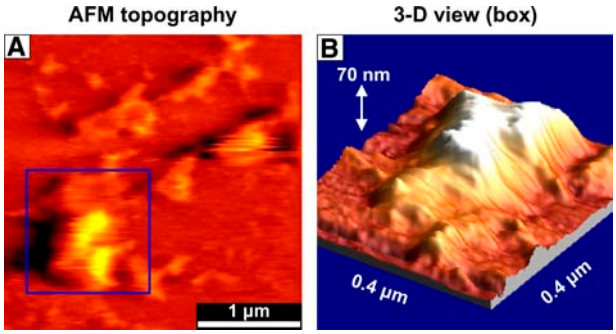

FIGURE 6 (*A*) AFM image at higher resolution of a resting RBL cell membrane sheet (clathrin labeled) showing several raised domains. (*B*) One domain (0.4 μm box) was selected for 3-D representation to highlight possible clathrin pits within the domain.

ranges from 15 nm to as much as 90 nm. By comparison, the flatter regions of these native membranes between the domains have an average thickness of ~7 nm, measured relative to the poly-L-lysine-coated substrate. (The edge of a membrane can be seen in Fig. 3 *A*.) This is not much greater than the 4.5 nm thickness of a typical model lipid bilayer (27) and is comparable to the 6.3 nm thickness measured for protein-containing ''purple membranes'' of *Halobacterium salinarum* (21). Thus the raised domains are significant protrusions that are much larger than the overall membrane thickness.

Cholesterol depletion reduces the height of raised domains

Cholesterol is a key component of the plasma membrane (28) and its loss has profound effects, including changes in recovery of specific components in light fractions of sucrose density gradient used as a biochemical measure of membrane raft integrity. Cholesterol depletion prohibits the formation of coated pits (29), leaving the membrane studded with flat clathrin arrays (*arrow*, Fig. 7 *D*) that cannot deliver cargo to the cell interior. Membrane perturbations associated with cholesterol depletion have frequently been used as an indicator of raft involvement (30,31). To determine the effects of cholesterol depletion on the topography of the cytoplasmic face, we incubated RBL cells with 10 μM MβCD for 30 min at 37°C before fixing cells and preparing membrane sheets for AFM measurements. Representative results in Fig. 7 demonstrate that the height of the raised domains on RBL membrane sheets is markedly reduced by cholesterol depletion. When analyzed in line profile or cross section (*red lines* in Fig. 7, *A* and *B*), a representative raised domain in control membranes has a peak height of almost 70 nm. By comparison, cross sectional analysis of a representative raised domain in a cholesterol-depleted membrane has a peak height of only 20 nm (*black lines* in Fig. 7, *A* and *C*). Analyses of repeated measurements are summarized in Table 1 and Fig. 9. Importantly, the loss of cholesterol fails to significantly alter the 7 nm thickness of the flat regions of membrane.

Cholesterol is observed in TEM dark patches

In prior work, x-ray spectral analysis of dried membrane sheets indicated that the dark patches have higher levels of carbon than bulk membrane (2). This result suggested that they contain a higher density of proteins and associated lipids and/or cholesterol than the surrounding membrane.

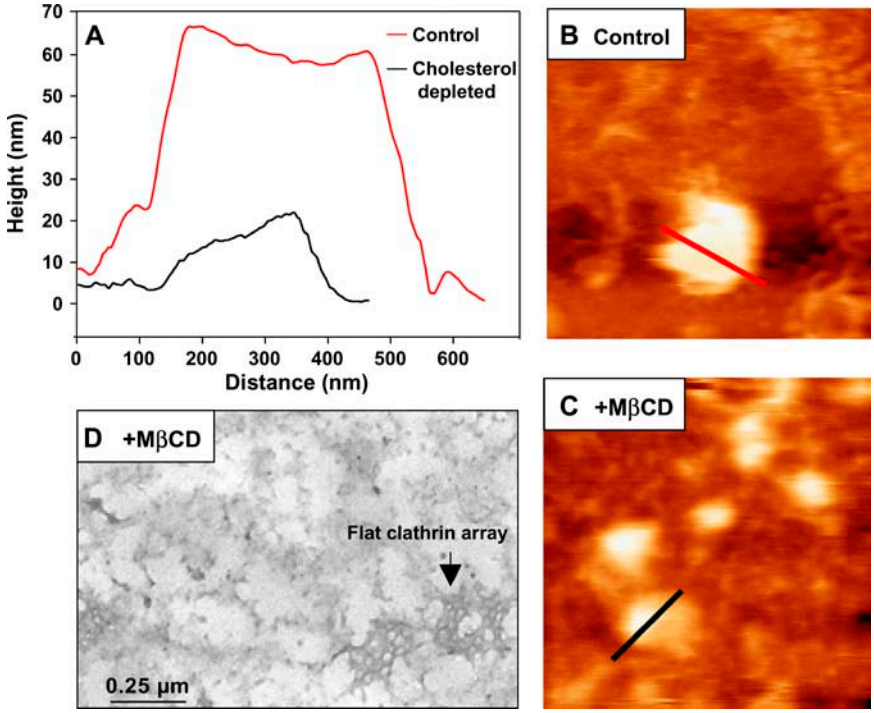

FIGURE 7 (*A*) Example of AFM topographic line profiles of raised domains for both control RBL cell membrane sheets (*B*) and those treated with 10 μM MβCD (*C*). The measurements show that the height of individual domains is substantially lower in cholesterol-depleted membranes (*black line*) than in control membranes (*red line*). The data for all the sheets studied are summarized in Table 1 and in histograms of Fig. 9. The data are independent of labeling. Image *B* was from a resting cell and image *C* was from an activated cell. A representative TEM image of cholesterol-depleted membranes is shown in *D*, where ''flattened'' clathrin arrays can be observed.

Fig. 8 shows two TEM images that support the concept that cholesterol is an important component of the dark patches and is thus in good agreement with their coidentity with the cholesterol-sensitive raised regions seen by AFM. In Fig. 8, *A* and *B*, membrane sheets from control and MβCD-treated cells were labeled with 5 nm gold particles coated with a monomeric form of PFO (32). A toxin produced by *Clostridium perfringens*, PFO specifically binds cholesterol and has been successfully used as a cytochemical probe for electron microscopy (33). In the control cells (Fig. 8 *A*), cholesterol is present in bulk membrane but is markedly clustered in a large darkened region (*arrow*, *lower left*). There is very little label in the MβCD-treated (cholesterol-depleted) cells (Fig. 8 *B*). Thus the dark patches contain high levels of cholesterol as well as proteins.

Quantifying the dimensions of the raised regions

The data above show that raised domains are a consistent feature of all the membrane sheet preparations studied by AFM to date. In Fig. 9, eight normalized histograms provide an expanded analysis of the raised domain heights and widths. The height and width data are broken down into activated and resting and with and without the MβCD treatment that extracts cholesterol. The histogram data are also condensed in Table 1, which includes the number of measurements for each structure. We see an increase in both the heights and widths of the raised domains for activated cells relative to resting cells. This is consistent with TEM observations (2,16,17) of protein recruitment to the dark patches. We see the same trend after MβCD treatment, which reduces the height of all raised domains but does not appear to reduce domain widths. It is important to note that concerning domain widths, the skewed histograms and large ranges are most likely due to aggregates of smaller domains. This would also reduce correlation, if any, between height and widths.

We note that these measurements were made using sheets labeled with IgE alone and also with sheets exposed to DNP-BSA and CTX-B on the extracellular side and with Abs to clathrin on the cytoplasmic side. To address the concern that these various labels would add substantial thickness to the membranes, we compared domain heights between membranes from resting cells that were unprimed with IgE relative to those that were and between membranes from activated cells that were labeled with primary and secondary antibodies for clathrin relative to those that were not. We found no statistical difference in the height of resting cells that were unprimed with IgE relative to those that were. We found that the clathrin labels added no more than 13 ± 5 nm to the domain height. In short, we attribute the domain heights to protein clustering and associated cholesterol and very little, if any, to the labels.

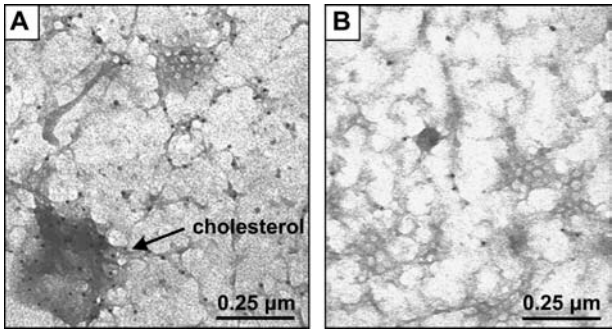

FIGURE 8 Distribution of PFO conjugated to 5 nm gold nanoparticles on RBL cell membrane sheets seen by TEM. On sheets from control cells (*A*), the abundant PFO label associates preferentially, but not exclusively, with darkened membrane (*arrow*). After treatment with 10 μM MβCD (*B*), only a few gold particles remain, demonstrating specificity of the PFO binding.

Linking raised domains to the cytoskeleton

The relationship between membrane signaling domains and the cytoskeleton is of great interest (34). Diffusion confinement zones have been attributed to the cytoskeleton (35,36). In the mast cell membrane, the cortical cytoskeleton forms a continuous submembranous meshwork (37). This meshwork is frequently observed on the inner surface of native membrane sheets in TEM images, where it seems to connect the darkened membrane areas (Fig. 10 *C;* also Fig. 8 *A*). Previous studies showed that the fibers bind phalloidin-gold particles and thus contain F-actin (16). When imaged by the AFM (Fig. 10, *A* and *B*), similar networks of fibers (*white arrows*) can be seen to surround and connect the raised domains. This supports the concept that the topography of the inner membrane is organized in part by the cortical cytoskeleton. We note that the cytoskeletal fibers are not seen in every AFM or TEM image of membrane sheets, whereas conventional thin section TEM shows a continuous actin meshwork under the mast cell membrane (37). Thus it is likely that a variable degree of cytoskeletal disassembly occurs during the membrane sheet preparation.

SUMMARY AND CONCLUSIONS

We have used simultaneous AFM and confocal fluorescence imaging of the cytoplasmic surface of membranes stripped from both resting and activated RBL-2H3 cells to reveal the presence of distinct membrane features (raised domains) that have the ability to concentrate numerous membrane molecules, including cross-linked receptors, gangliosides, and clathrin. Raised domains are found in the membrane of both resting and activated cells. The principal effect of cell activation is to cause the reorganization of membrane components into larger domains. Based upon AFM measurements of their thickness, lipid phase changes are unlikely to contribute substantially to these raised domains. We suggest instead that they represent areas that concentrate transmembrane and peripheral membrane proteins, either constitutively or inducibly, and that their bulky cytoplasmic tails and associated binding partners contribute to the height. Another significant

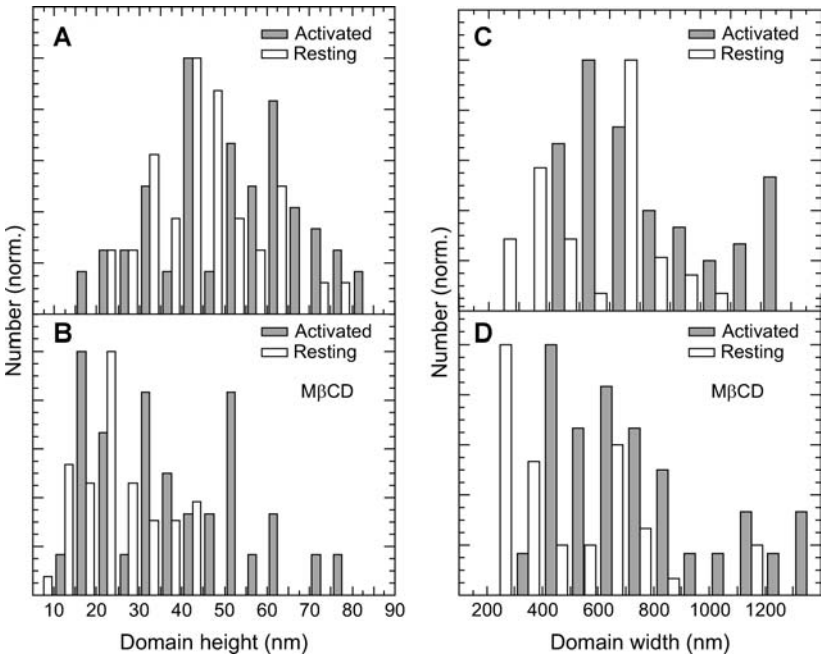

FIGURE 9 Histogram display of distributions of raised domain heights and widths as measured by cross section (illustrated in Fig. 7). The data incorporate all the membrane sheets in this study and were independent of cell labeling by IgE, CTX-B, or clathrin. The clathrin label (mouse monoclonal anti-clathrin heavy chain and Alexa 488 $F(ab')_2$ goat anti-mouse IgG) adds ~13 nm to the domain height. Histogram *A*(*C*) shows the distribution of domain heights(widths) for activated (*shaded bars*) and resting (*open bars*) membrane sheets. Histogram *B*(*D*) is the distribution of heights(widths) for membranes subjected to cholesterol extraction by MβCD.

contributor to the thickness may be clathrin lattices and clusters of clathrin-coated pits.

Based on composition, we conclude that the raised domains seen by AFM correspond to the dark patches observed in TEM images of signaling domains that also localize the immunoreceptor, FcεRI, at least 10 associated signaling molecules, and also molecules involved in coated pit assembly to dark regions of activated mast cell membranes (16,17). Concentrated proteins could explain in part the increased amount of carbon found by x-ray spectral imaging in the darkened patches (2).

We showed by TEM that the cholesterol marker PFO preferentially binds darkened membranes and by AFM that cholesterol extraction by MβCD causes a large reduction in height of the raised domains. These complementary results indicate that cholesterol contributes significantly to the formation or stability of the raised domains. The mechanism is not known with certainty. It is possible that MβCD reduces domain height by extracting not only cholesterol but also proteins in the form of protein-cholesterol complexes. Another possibility is that the recruitment of signaling proteins to the domains is reduced in the absence of cholesterol. Additionally, we have observed by EM that the inner membrane of MβCD-treated cells is enriched in flat clathrin arrays but is totally lacking in coated vesicles (Fig. 7 *D*). If much of the height is due to the curvature of 3-D clathrin lattices, cholesterol extraction would appear to ''flatten'' those structures.

The apparent relationship of the raised domains to the cytoskeleton (Fig. 10) is of particular interest. Previous fluorescence recovery after photobleaching data (38) and SPT data (35,36) have led to models that consider roles for cytoskeletal ''fences'' or ''corrals'' and anchored protein ''pickets'' in the temporary, dynamic confinement of membrane proteins and lipids and also in the formation of less mobile macromolecular complexes during signaling. In particular, the SPT studies typically reveal free diffusion of proteins and lipids within 40–700 nm confinement zones accompanied by infrequent intercompartmental transitions (''anomalous diffusion'', ''hop diffusion''). However, particularly for particles linked

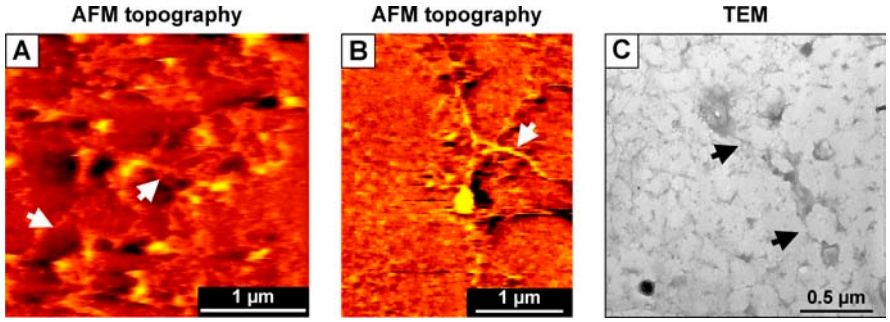

FIGURE 10 (*A* and *B*) AFM topography of RBL cell membrane sheets where cytoskeleton cables (*white arrows*) appear to link numerous raised domains. The maximum height in *A* is 54 nm and the maximum height in *B* is 45 nm. (*C*) Cytoskeleton cable linkages (*black arrows*) appear in a TEM image.

to lipids, it has never been clear why interactions of the cytoskeleton with components of the inner leaflet of the membrane bilayer would regulate mobility in the outer leaflet of the bilayer. The AFM images presented here show cytoskeletal elements surrounding and connecting the raised domains. These images thus raise the possibility that the cortical cytoskeleton may determine the stability and characteristics of membrane domains, which in turn may determine the ability of proteins (and lipids) to access and escape from these specialized regions.

In summary, AFM/fluorescence imaging of the inner membrane landscape has revealed levels of topographical complexity that are not addressed either in the well-mixed lipid and protein model proposed by Singer and Nicholson (1) or in progressively more complex models developed over the subsequent decades that incorporate concepts of compositional and functional heterogeneity within the membrane bilayer and between the membrane and the cytoskeleton (34). Further analysis of the composition of distinct membrane compartments across the topographic landscape is expected to reveal new insight into the relationship of membrane geometry to membrane molecular organization and function.

Sandia is a multi-program laboratory operated by Sandia Corporation, a Lockheed Martin Company, for the U.S. Dept. of Energy under contract DE-AC04-94AL85000. Use of the electron microscopy facilities at the University of New Mexico-Health Sciences Center is gratefully acknowledged.

This work was supported in part by National Institutes of Health grants P20GM66283, R01GM49814, and R01AI051575 and in part by the Division of Materials Science, Office of Basic Energy Sciences, U.S. Dept. of Energy.

REFERENCES

1. Singer, S., and G. Nicolson. 1972. The fluid mosaic model of the structure of cell membranes. *Science*. 175:720–731.
2. Wilson, B., S. Steinberg, K. Liederman, J. Pfeiffer, Z. Surviladze, J. Zhang, L. Samelson, L. Yang, P. Kotula, and J. Oliver. 2004. Markers for detergent-resistant lipid rafts occupy distinct and dynamic domains in native membranes. *Mol. Biol. Cell*. 15:2580–2592.
3. Oliver, J., and R. Berlin. 1982. Mechanisms that regulate the structural and functional architecture of cell surfaces. *Int. Rev. Cytol*. 74:55–94.
4. Jacobson, K., E. Sheets, and R. Simson. 1995. Revisiting the fluid mosaic model of membranes. *Science*. 268:1441–1442.
5. Lai, E. 2003. Lipid rafts make for slippery platforms. *J. Cell Biol*. 162: 365–370.
6. Edidin, M. 2003. The state of lipid rafts: from model membranes to cells. *Annu. Rev. Biophys. Biomol. Struct*. 32:257–283.
7. Edidin, M. 2001. Shrinking patches and slippery rafts: scales of domains in the plasma membrane. *Trends Cell Biol*. 11:492–496.
8. Brown, D., and E. London. 1998. Functions of lipid rafts in biological membranes. *Annu. Rev. Cell Dev. Biol*. 14:111–136.
9. Field, K., D. Holowka, and B. Baird. 1995. FcεRI-mediated recruitment of p53/56^{lyn} to detergent-resistant membrane domains accompanies cellular signaling. *Proc. Natl. Acad. Sci. USA*. 92:9201–9205.
10. Koumanov, K., C. Tessier, A. Momchilova, C. Rainteau, C. Wolf, and P. Quinn. 2005. Comparative lipid analysis and structure of detergent-resistant membrane raft fractions isolated from human and ruminant erythrocytes. *Arch. Biochem. Biophys*. 434:150–158.
11. Douglass, A., and R. Vale. 2005. Single-molecule microscopy reveals plasma membrane microdomains created by protein-protein networks that exclude or trap signaling molecules in T cells. *Cell*. 121:937–950.
12. Friedrichson, T., and T. Kurzchalia. 1998. Microdomains of GPI-anchored proteins in living cells revealed by crosslinking. *Nature*. 394: 802–805.
13. Varma, R., and S. Mayor. 1998. GPI-anchored proteins are organized in submicron domains at the cell surface. *Nature*. 394:798–801.
14. Pralle, A., P. Keller, E. Florin, K. Simons, and J. Horber. 2000. Sphingolipid-cholesterol rafts diffuse as small entities in the plasma membrane of mammalian cells. *J. Cell Biol*. 148:997–1007.
15. Prior, I., C. Muncke, R. Parton, and J. Hancock. 2003. Lipid rafts: heterogeneity on the high seas. Direct visualization of Ras proteins in spatially distinct cell surface microdomains. *J. Cell Biol*. 160: 165–170.
16. Wilson, B., J. Pfeiffer, and J. Oliver. 2000. Observing FcεRI signaling from the inside of the mast cell membrane. *J. Cell Biol*. 149:1131–1142.
17. Wilson, B., J. Pfeiffer, Z. Surviladze, E. Gaudet, and J. Oliver. 2001. High resolution mapping reveals distinct FcεRI and LAT domains in activated mast cells. *J. Cell Biol*. 154:645–658.
18. Müller, D., D. Fotiadis, and A. Engel. 1998. Mapping flexible protein domains at subnanometer resolution with the atomic force microscope. *FEBS Lett*. 430:105–111.
19. Müller, D., J. Heymann, F. Oesterhelt, C. Möller, H. Gaub, G. Büldt, and A. Engel. 2000. Atomic force microscopy of native purple membrane. *Biochim. Biophys. Acta*. 1460:27–38.
20. Czajkowsky, D., and Z. Shao. 1998. Submolecular resolution of single macromolecules with atomic force microscopy. *FEBS Lett*. 430: 51–54.
21. Stark, M., C. Möller, D. Müller, and R. Guckenberger. 2001. From images to interactions: high resolution phase imaging in tapping-mode atomic force microscopy. *Biophys. J*. 80:3009–3018.
22. Dufrêne, Y., W. Barger, J.-B. Green, and G. Lee. 1997. Nanometer-scale surface properties of mixed phospholipid monolayers and bilayers. *Langmuir*. 13:4779–4784.
23. Burns, A. 2003. Domain structure in model membrane bilayers investigated by simultaneous atomic force microscopy and fluorescence imaging. *Langmuir*. 19:8358–8363.
24. Burns, A., D. Frankel, and T. Buranda. 2005. Local mobility in lipid domains of supported bilayers characterized by atomic force microscopy and fluorescence correlation spectroscopy. *Biophys. J*. 89:1081–1093.
25. Liu, F., J. Bohn, E. Ferry, C. Yamamoto, C. Molinaro, L. Sherman, N. Klinman, and D. Katz. 1980. Monoclonal dinitrophenyl-specific murine IgE antibody–preparation, isolation, and characterization. *J. Immunol*. 6:2728–2737.
26. Sanan, D., and R. Anderson. 1991. Simultaneous visualization of LDL receptor distribution and clathrin lattices on membranes torn from the upper surface of cultured cells. *J. Histochem. Cytochem*. 39:1017–1024.
27. Nagle, J., and J. Tristam-Nagle. 2000. Structure of lipid bilayers. *Biochim. Biophys. Acta*. 1469:159–195.
28. Maxfield, F., and D. Wustner. 2002. Intracellular cholesterol transport. *J. Clin. Invest*. 110:891–898.
29. Subtil, A., I. Gaidarov, K. Kobylarz, M. Lampson, J. Keen, and T. McGraw. 1999. Acute cholesterol depletion inhibits clathrin-coated pit budding. *Proc. Natl. Acad. Sci. USA*. 96:6775–6780.
30. Lawrence, J., D. Saslowsky, J. Edwardson, and R. Henderson. 2003. Real-time analysis of the effects of cholesterol on lipid raft behavior using atomic force microscopy. *Biophys. J*. 84:1827–1832.
31. Romanenko, V., Y. Fang, F. Byfield, A. Travis, C. Vandenberg, G. Rothblat, and I. Levitan. 2004. Cholesterol sensitivity and lipid raft targeting of Kir2.1 channels. *Biophys. J*. 87:3850–3861.

32. Ramachandran, R., R. Tweten, and A. Johnson. 2005. The domains of a cholesterol-dependent cytolysin undergo a major FRET-detected rearrangement during pore formation. *Proc. Natl. Acad. Sci. USA.* 102: 7139–7144.

33. Fujimoto, T., M. Hayahi, M. Iwamoto, and Y. Ohnoiwashita. 1997. Crosslinking plasmalemmal cholesterol is sequestered to caveolae: analysis with a new cytochemical probe. *J. Histochem. Cytochem.* 45: 1197–1205.

34. Vereb, G., J. Szöllosi, J. Matkó, P. Nagy, T. Farkas, L. Vígh, L. Mátyus, and T. Waldmann. 2003. Dynamic, yet structured: the cell membrane three decades after the Singer-Nicolson model. *Proc. Natl. Acad. Sci. USA.* 100:8053–8058.

35. Dietrich, C., B. Yang, T. Fujiwara, A. Kusumi, and K. Jacobson. 2002. Relationship of lipid rafts to transient confinement zones detected by single particle tracking. *Biophys. J.* 82:274–284.

36. Murase, K., T. Fujiwara, Y. Umemura, K. Suzuki, R. Iino, H. Yamashita, M. Saito, H. Murakoshi, K. Ritchie, and A. Kusumi. 2004. Ultrafine membrane compartments for molecular diffusion as revealed by single molecule techniques. *Biophys. J.* 86:4075–4093.

37. Pfeiffer, J., G. Deanin, J. Seagrave, B. Davis, and J. Oliver. 1985. Membrane and cytoskeletal changes associated with IgE-mediated serotonin release in rat basophilic leukemia cells. *J. Cell Biol.* 101:2145–2155.

38. Tang, Q., and M. Edidin. 2003. Lowering the barriers to random walks on the cell surface. *Biophys. J.* 84:400–407.

Distribution

3	MS 1413	A. R. Burns, 8831
1	MS 1413	P. V. Dressendorfer, 8331
2	MS 9018	Central Technical Files, 8944
2	MS 0899	Technical Library, 4536